Journal of Marine Systems 83 (2010) 221–241

Contents lists available at ScienceDirect

Journal of Marine Systems

journal homepage: www.elsevier.com/locate/jmarsys

An emergent community ecosystem model applied to the California Current System

Nicole L. Goebel [a], Christopher A. Edwards [b,*], Jonathan P. Zehr [b], Michael J. Follows [c]

[a] Institute of Marine Sciences, University of California, Santa Cruz, CA 95064, USA
[b] Ocean Sciences Department, University of California, Santa Cruz, CA 95064, USA
[c] Department of Earth, Atmospheric and Planetary Sciences, Massachusetts Institute of Technology, Cambridge, MA 02139, USA

ARTICLE INFO

Article history:
Received 24 October 2009
Received in revised form 17 April 2010
Accepted 2 May 2010
Available online 11 May 2010

Keywords:
Ecosystem
Modeling
California Current System

ABSTRACT

An ecosystem model that supports considerable phytoplankton diversity is coupled to a circulation model of the California Current System. The Regional Ocean Modeling System is configured for a realistic simulation at 0.1° resolution for years 2000–2004. The concentration-based ecosystem model includes multiple nutrients, dissolved and particulate organic pools, two grazers, and 78 phytoplankton organism. Primary producers divide into 4 functional groups representing diatoms, large phytoplankton that do not require silicate, *Prochlorococcus*-like organisms, and small phytoplankton that can use nitrate. Random selection of phytoplankton growth parameters creates an autotrophic community able to fill multiple environmental niches created by the physical circulation and plankton population. In the 5-year average, over 98% of the total biomass at the surface is contained within 8 primary producers, with 30 additional phytoplankton sustained at lower levels. Modeled surface phytoplankton biomass is evaluated on multi-annual and seasonal bases using satellite chlorophyll estimates for the same period. The self-organized communities produced by the model represent various features of the California Current Ecosystem, including the biogeographic break at Pt. Conception. The annual average fields generally reveal high diatom concentrations nearshore, with small phytoplankton more broadly distributed. *Prochlorococcus*-like organisms are absent or at relatively low concentrations at the coast, increasing across the California Current. Small non-*Prochlorococcus*-like phytoplankton types are found at highest concentrations nearshore and far offshore. The model exhibits both surface and subsurface features, including a seasonal subsurface chlorophyll maximum along CalCOFI Line 77 between May and October. Time-series of area averaged model fields show seasonal progressions of different phytoplankton groups.

1. Introduction

One challenge for modeling ocean ecosystems is representing the remarkable diversity of marine planktonic organisms. In nature, such diversity is revealed by observations of multiple species at varying biomass concentrations and having differing community structure within spatially or temporally distinct biogeographical domains. Ever improving observational approaches have over time increased documentation of oceanic species. Identifying subspecies differentiation is now routine through the use of molecular techniques. How such diversity in the ocean is sustained given the small number of limiting nutrients remains a long-standing scientific question (Hutchinson, 1961; Roy and Chattopadhyay, 2007), and our understanding of its impact on overall ecosystem dynamics and net biological production remains incomplete. If ecosystem models are able to represent the complex heterogeneous planktonic diversity in the ocean, they represent one method to investigate and better understand the underlying causes and impacts.

Historically, concentration-based ocean ecosystem models have addressed biodiversity minimally, typically budgeting phytoplankton, for example, through the use of one or a small number of functional groups that implicitly represent many different phytoplankton species. Among the simplest of these models is the *NPZ* model (e.g., Franks et al., 1986), which includes one nutrient (*N*), one phytoplankton type (*P*), and one zooplankton (*Z*). More complex variants add detritus (Powell et al., 2006) to this framework, and Gruber et al. (2006) include two nutrient and two detrital compartments. Other models (e.g., Chai et al., 2002; Moore et al., 2002a; Litchman et al., 2006) expand phytoplankton into two functional groups and zooplankton into one, two, or three boxes. All models described have been valuable tools to study ocean ecosystems in different contexts, and choosing the appropriate level of model complexity has been considered typically on a problem dependent basis. Taken as a series, these examples highlight the fact that over decades traditional ecosystem models have evolved in systematic but incremental progression, resolving only a very small amount of total planktonic diversity.

An alternate approach toward ecosystem model construction has been developed recently (Follows et al., 2007). At its core, this type of emergent community ecosystem model is not fundamentally

* Corresponding author.
E-mail addresses: ngoebel@ucsc.edu (N.L. Goebel), cedwards@ucsc.edu (C.A. Edwards), zehrj@pmc.ucsc.edu (J.P. Zehr), mick@ocean.mit.edu (M.J. Follows).

0924-7963/$ – see front matter © 2010 Elsevier B.V. All rights reserved.
doi:10.1016/j.jmarsys.2010.05.002

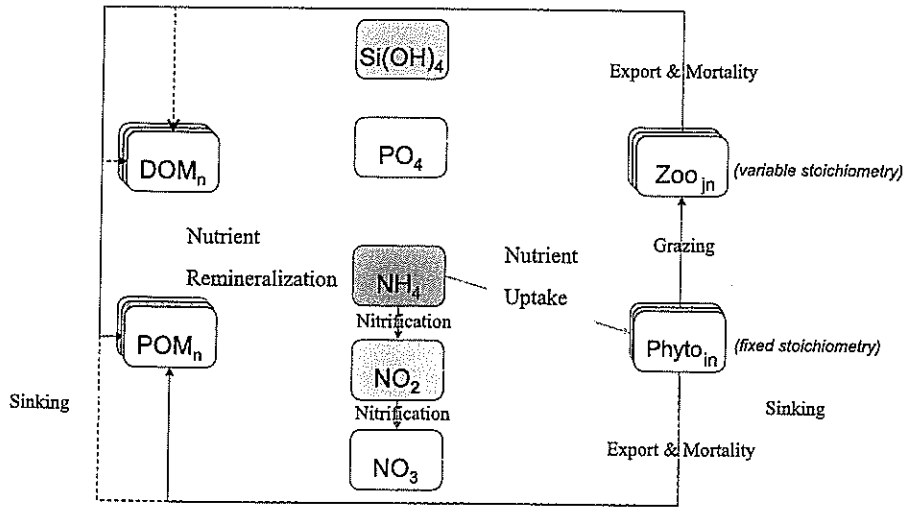

Fig. 1. Ecosystem model conceptual diagram. Boxes represent different state variables. Colors correspond to nutrient type. Arrows represent processes as labeled. The subscript n refers to the specific nutrient for DOM, POM, Zoo and Phyto state variables. The subscript i and j represent the index of phytoplankton or zooplankton analog. (For interpretation of the references to color in this figure legend, the reader is referred to the web version of this article.)

different from the more traditional type. It solves a series of coupled nonlinear differential equations quantifying changes in time for biological and chemical concentrations with formulations similar to other models. However, this approach is unique both in the large number (O(100)) of viable phytoplankton fields included and in the method by which some rate-controlling parameters are set.

In traditional *NPZ*-type models, parameters that control growth, grazing, and remineralization processes are precisely chosen by the modeler. At times, this selection is made with careful attention to observations or field studies appropriate for a particular region (Banas et al., 2009), but some parameters (e.g., zooplankton mortality) are not easily measured, and the value used is less constrained. Other parameters, such as the sensitivity of growth rate to ambient temperature, show substantial scatter (Eppley, 1972; Brush et al., 2002); choosing a single value may not represent the breadth of values found in nature within a functional group (Moisan et al., 2002). Furthermore, underlying model evolution can be sensitive to parameter choice (Edwards et al., 2000b). In the Follows et al. (2007) approach, some rate-controlling parameters are fixed as in more traditional cases, but others are randomly chosen within reasonable limits given observational scatter. Thus the model ocean is seeded with a large number of independent phytoplankton species or subspecies, each with its own growth parameters and able to compete individually for available resources. Applied to the global ocean, this model resolved latitudinal structure for 3 ecotypes of *Prochlorococcus* spp. similar to that found along the Meridional Atlantic Transect (Johnson et al., 2006; Follows et al., 2007). The modeled structure derived from differing temperature and light environments in different oceanic regions combined with the availability within the model of organisms able to utilize resources efficiently in the differing environmental niches. The diversity of autotrophic microbial populations and underlying processes have typically been neglected by more traditional modeling exercises, and the Follows et al. (2007) model is among the first to represent these explicitly in a fully prognostic fashion.

Like their global ocean counterparts, coastal regions also exhibit a range of chemical and physical environments owing to the presence of an oceanic boundary and the changes with cross-shore distance in the large-scale circulation, mesoscale variability, sub-mesoscale motion, and vertical mixing. The California Current System (CCS), off the west coast of the United States, includes such variations in oceanic environments, and evidence suggests considerable planktonic diversity regionally, particularly between seasonally varying, often nutrient replete, upwelled waters nearshore and oligotrophic offshore waters (e.g., Venrick, 2009).

In this paper, we investigate the potential for the Follows et al. (2007) model to represent the biogeography and biodiversity of the California Current System. The model is seeded with 78 viable phytoplankton types that can be collated into four functional groups. Physiological traits (e.g., nutrient utilization and affinity, and response to temperature and light) for each phytoplankton are randomly assigned from a range of values drawn from the literature. With this approach, multiple, viable phytoplankton types compete for resources, enabling a self-organizing phytoplankton community to emerge. In Section 2 we describe the model, its components, and both fixed and randomized biological parameterizations. Section 3 presents results, including a quantitative model evaluation and descriptions of the surface and subsurface fields, both time-averaged and over an annual cycle. We conclude in Section 4 with a discussion of the results in context with CCS observations.

2. Model formulation

2.1. Emergent community ecosystem model

The ecosystem model is derived from the original, global-scale version of Follows et al. (2007). The model is schematically shown in Fig. 1. Multiple phytoplankton populations access five inorganic nutrients (NO_3, NO_2, NH_4, PO_4, and $Si(OH)_4$) and are grazed by two different sized zooplankton. Transfers from phytoplankton and zooplankton populations to dissolved and detrital pools represent respiration, mortality, excretion, and sloppy feeding. Dissolved and detrital constituents are remineralized into inorganic form. The equations that govern the evolution of the ecosystem components are provided in the Appendix and parameters are presented in Tables A.1, A.2, and A.3.

Our model is seeded with 78 individual phytoplankton types that are randomly subdivided.[1] Phytoplanktons species are first divided approximately equally into small and large size classes. Large phytoplankton are similarly subdivided into one group, representing diatoms, that require silicate for growth, and a second category, referred to as LND (large non-diatoms), that does not use silicate. Small phytoplankton are split into three different groups according to their

[1] The number 78 derives from early versions of this model which were constrained to have less than 100 total tracer variables and has no additional significance.

nitrogen utilization. Roughly one third of small phytoplankton uses both NH_4 and NO_2, one third uses NH_4 only, and the remainder can take up NH_4, NO_2, and NO_3. We refer to these small phytoplankton as SP1, SP2, and SP3, respectively. For analysis described in this paper, SP1 and SP2 are grouped into a category referred to as PLP (*Prochlorococcus*-like phytoplankton), which are thought to primarily use NH_4 and NO_2 (Moore et al., 2002b). SP3 is assumed to include all other small prokaryotes and eukaryotes, and we refer to this group as SNP (Small Non-*Prochlorococcus*-like). For clarity below, we refer to organisms within a particular functional group as subtypes as our categorization cannot distinguish between different ecotypes of a single species and entirely different taxa within a particular functional group.

Large phytoplankton types are assigned faster maximum growth rates than small phytoplankton. Diatoms are an important functional group in coastal upwelling systems, and studies frequently report diatom growth rates that exceed the community average (Chan, 1978, 1980; Brand, 1981; Brand and Guillard, 1981; Furnas, 1990, 1991). For diatoms, we use a maximum diel-averaged growth rate of approximately 3.6 divisions per day, near the upper end of the net growth rates reported by Furnas (1990). Studies of maximum net growth rate for large non-diatoms, such as dinoflagellates, have been found in the same range but generally lower than that of diatoms (Chan, 1978; Weiler and Eppley, 1979; Chan, 1980), and our value corresponds to a maximum 2.9 doublings per day. Small phytoplankton are allowed to divide at a maximum of 2 times per day; this value is somewhat higher than that implied by the culture experiments for *Synechococcus* and *Prochlorococcus* (Moore et al., 2002b), but similar to the maximum net growth rates for picoeukaryotes in dilution-based studies by (Worden et al., 2004).

We note that the maximum growth rates listed in Table A.1 are twice those normally reported and implied by the preceding discussion; however, in our model these values result in approximately equivalent daily averaged growth. Phytoplankton growth depends on incident photosynthetically active radiation which undergoes diel variations in our model configuration. Literature-based rates are obtained usually from laboratory measurements over a 24-hour period. Fig. 2 compares the time-evolution of phytoplankton biomass for two simplified models including only uptake and respiration (no grazing). In both experiments, nutrients are plentiful, and the respiration rate is 0.1 d^{-1}. The dashed curve results from a growth rate of 1.4 d^{-1} and a light field that is constant with time. The solid curve corresponds to a growth rate of 2.8 d^{-1} but with a light field that varies as a step function between day and night cycles (dotted line). While respiration occurs at all times (Marra and Barber, 2004), it is most evident in the solid curve during nighttime. It is clear that the net increase in phytoplankton biomass in our two experiments is roughly equivalent over multiple days of growth.

Generally, realized phytoplankton growth is less than the maximum possible rate resulting from modeled limitations associated with nutrient concentrations, ambient temperature, and local light intensity. The four parameters that control these environmental responses are the half saturation constants for uptake of each nutrient (generically referred to here as k_x), a temperature optimum (T_o) and two light optimum parameters (k_{inh} and k_{par}). These parameters are determined randomly within limits for each phytoplankton analog.

Nutrient limitation by inorganic phosphate and silicic acid is expressed using Michaelis–Menten kinetics. Inorganic nitrogen limitation is functionally similar, but quantitatively determined for each form of nitrogen assimilated. Oxidized forms of nitrogen are theorized to be more energetically expensive to assimilate, and their uptake is inhibited by the presence of ammonium in the model (Nianzhi, 1993; L'Helguen et al., 2008). Phytoplankton growth is reduced by the most limiting nutrient resource. Half saturation constants for phosphorus are related to those for nitrate and nitrite by a fixed Redfield Ratio. Half saturation constants for ammonium are one half those for nitrite or nitrate; a higher affinity for NH_4 than NO_3 (Dugdale and Goering, 1967; Eppley et al., 1969; Conway, 1977) has been reported in small phytoplankton such as green algae (Litchman et al., 2007). The half saturation constant for silicate is fixed for diatoms, while that for phosphorus and other stoichiometrically related nutrients are drawn from uniform distributions having size-dependent ranges (Table A.1). Large phytoplankton typically have higher k_x than small phytoplankton (Eppley et al., 1969).

Realized phytoplankton growth is also modified by local temperature, with warmer conditions generally enabling faster growth rates.

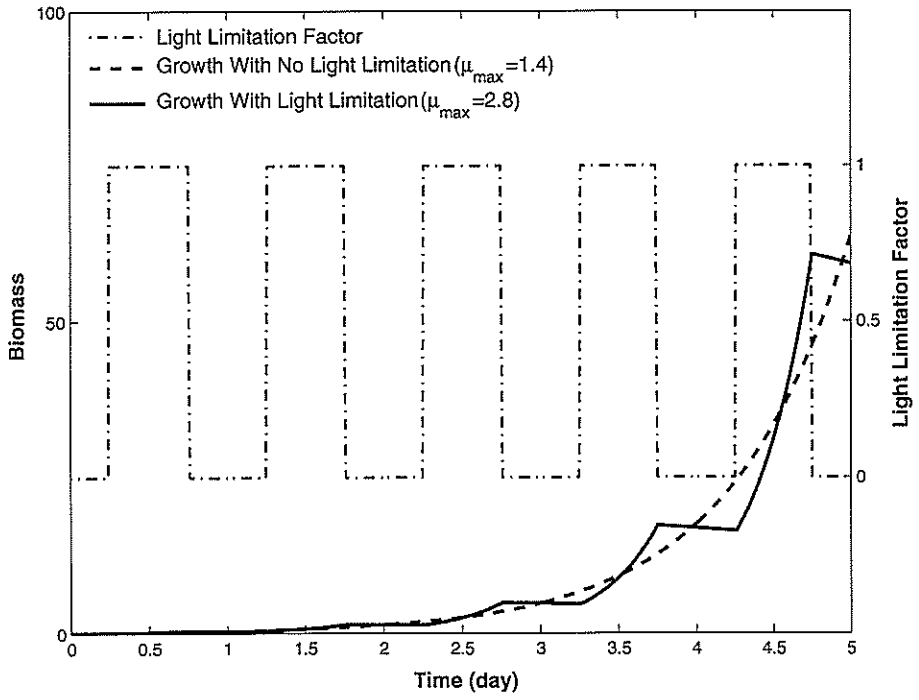

Fig. 2. Left axis: Time series of phytoplankton biomass for a model of phytoplankton subject to growth and respiration under continuous irradiance (dashed) and with a 12-hour on/12-hour off cycle (solid). Growth rate is 1.4 d^{-1} (2.8 d^{-1}) for dashed (solid) growth curve. Right axis: light limitation factor that corresponds to solid curve.

However, each phytoplankton analog is individually and randomly prescribed a temperature optimum, T_o. This value, along with a specified temperature decay scale, T_d, defines a phytoplankton-specific temperature window for growth within a broader temperature limitation curve. The optimum is drawn from a uniform distribution between specified minimum and maximum temperatures characteristic of the CCS (Table A.1). This approach generates warm and cold adapted phytoplankton types in both size classes.

Finally, light limitation of phytoplankton growth is determined by the local photosynthetically active radiation and two parameters: k_{par} governs the limitation function under low-light conditions, and k_{inh} controls growth when solar radiation is high. Chloroplast placement due to packaging effects observed in large phytoplankton (Finkel, 2001) justifies a high light optimum (i.e., low k_{inh} and a narrow range of k_{par}). Small phytoplankton have been observed to grow optimally at a wider range of light levels due to the presence of both high and low-light adapted strains (Veldhuis et al., 2005), and therefore were assigned a wider range of light optima. The distributions from which light parameters for large and small phytoplankton are drawn, however, overlap (Table A.1), and therefore such generalizations can occasionally be reversed. The light limitation model includes self-shading but does not resolve spectral bands.

For simplicity, the remaining ecosystem model parameters that describe phytoplankton losses (mortality, export and sinking) and heterotrophic processes (zooplankton grazing, sinking of detrital particulates, detrital and dissolved organic matter remineralization, and nitrification) are fixed rather than randomly prescribed. See Appendix A for the formulations.

Export and sinking of phytoplankton are size-specific. The rates for these processes are greater for large phytoplankton than for small phytoplankton. Mortality rates are set equal for all phytoplankton.

Two grazers are included in the model, and their parameters are not drawn from a random distribution of values. Change in biomass for each zooplankton is modeled using a sigmoidal grazing scheme (Gentleman et al., 2003), dependent on a maximum grazing rate (G^{max}), assimilation efficiency (α), and prey palatability (π) (Table A.2). The maximum grazing rate is size-specific. Mesozooplankton G^{max} is smaller than the microzooplankton rate (e.g., Leising et al., 2005a). Grazing varies also with the palatability and assimilation efficiency of the prey. Microzooplankton and large non-diatoms are parameterized as highly palatable to mesozooplankton, and small phytoplanktons are highly palatable to microzooplankton. Diatoms are less palatable to all zooplankton within the model, due to their size, shape, ornamentation, exudates, and siliceous frustrule. Small phytoplankton populations are modeled as least palatable to mesozooplankton, and large phytoplankton are of medium palatability for microzooplankton. Assimilation efficiencies are highest for mesozooplankton consuming small phytoplankton, medium for phytoplankton grazing by like-sized zooplankton, and lowest for microzooplankton ingesting large phytoplankton. Grazing of microzooplankton by mesozooplankton is included providing potential relief of grazing pressure on the prey of the microzooplankton, as observed in nature (e.g., Leising et al., 2005b). Modeled zooplankton stoichiometry is allowed to vary, as opposed to the Redfield-based ratio of phytoplankton. Zooplankton mortality obeys a linear relationship with biomass.

In addition to the two explicitly modeled grazers, the heterotrophic component also includes an implicit representation of microbes that remineralize dissolved and particulate organic detrital pools that accumulate from the mortality and excretion of phytoplankton and zooplankton (Fig. 1). Remineralization of organic matter varies linearly with its concentration. Organic phosphorus is remineralized into phosphate, while organic nitrogen is remineralized into ammonium, which is then nitrified to nitrite and then to nitrate. Nitrification is modeled as a linear function with fixed coefficients (Table A.3). Rate parameters for remineralization processes are based on sensitivity tests of literature-based values. There is no dissolved organic silicate pool, and particulate silica is converted to the inorganic pool.

Overall, the underlying model equations are conservative and ensure that biological tracers are positive definite. The model coding maintains conservation and ensures that tracer levels do not fall below an extremely low, positive threshold. This threshold allows extremely small seed populations to remain viable for future potential growth.

For comparison to observed biomass estimates, modeled biomass in μmol phosphorus liter^{-1} is converted to carbon using a Redfield ratio and then to mg chlorophyll m^{-3} as follows. The carbon to chlorophyl ratio, C:Chl, is represented as a constant value for each functional group. Phytoplankton C:Chl ratios (as g C g chl^{-1}) reported in the literature range from values of 10 to more than 700. Interspecific variation in C:Chl ratios of phytoplankton have been shown to vary across conditions of light, nutrients, and temperature (Geider, 1987). C:Chl ratios within a functional group however, are relatively consistent, ranging from high values for oligotrophic, low-chlorophyll regions (Buck et al., 1996) and low values for larger phytoplankton in eutrophic environments (Geider, 1987). C:Chl ratios exceeding 300 have been observed in oligotrophic waters where small phytoplankton predominate (Buck et al., 1996; Chavez et al., 1996; Chang et al., 2003; Veldhuis and Kraay, 2004) and were observed to reach values of 300 in waters that contained only small phytoplankton cells (<5 μm) (Putland and Iverson, 2007). We used a C:Chl ratio of 300 to represent the small phytoplankton in our model. Diatom-specific C:Chl found throughout the literature falls within the lower range of ratios, from 15 to 46 (Chan, 1980; Geider, 1987; Gallegos and Vant, 1996), while the C:Chl ratio in eutrophic environments ranged from 16 to 83, most of which fell between 27 and 67 mg C mg chl^{-1} (Riemann et al., 1989; Sathyendranath et al., 2009). We represent coastal diatoms with a C:Chl ratio of 50, a middle value within this range. Reports of C:Chl ratios for dinoflagellates fall between that of small phytoplankton and large diatoms. Geider (1987) measured a range of 20 to 140and Chan (1980) measured a range of 90 to 120, while Sathyendranath et al. (2009) measured a range of 27 to 80 in Tokyo Bay. Based on these ranges for dinoflagellates which exceed those for diatoms, we apply a C:Chl of 100 for large non-diatoms. Gruber et al. (2006) applied a variable C:Chl ratio in their ecosystem model of the CCS. Resultant C:Chl in their model demonstrated onshore values of 40 and offshore values of 100, which fall within the ranges chosen here. Gruber et al. (2006) demonstrated the small benefit of utilizing a modeled C:Chl ratio when compared to using the average modeled value for the photic zone in instances where one is concerned only with surface chlorophyll concentrations. They found that a canonical, constant value of 40 would have largely impacted both the depth distributions and the relative onshore–offshore chlorophyll concentrations. In the present study, we also find a variable ratio important in estimating chlorophyll concentrations associated with small phytoplankton offshore, though this variability is expressed on a functional group basis in our model.

2.2. Physical model and coupled model conditions

The ecosystem model is embedded within a physical circulation model of the California Current System. We use the Regional Ocean Modeling System (ROMS) configured for the CCS. Our implementation extends from the middle of the Baja California Peninsula to Vancouver Island and over 1000 km offshore at 1/10° resolution and 42 vertical, topography-following levels. The model is forced at the surface by atmospheric fields from a high-resolution atmospheric model (COAMPS™, provided by the Naval Research Laboratory). Lateral boundary conditions are obtained from output from the global ocean state estimate ECCO (Estimating the Circulation and Climate of the Ocean). Details of the forward physical circulation model, its quantitative comparison to observations, and its sensitivities to local

and remote forcing are provided in Veneziani et al. (2009a,b). Additional information relating to how the forward model circulation changes as a result of regional data assimilation can be found in Broquet et al. (2009). The primary difference between the physical implementation in the present study and those previously documented is the application of a positive definite tracer advection scheme as opposed to a third-order upstream tracer advection. We use the Multidimensional Positive Definite Advection Transport Algorithm (MPDATA; Smolarkiewicz and Margolin, 1998). A positive definite scheme is particularly helpful for ecosystem model studies to eliminate negative tracer values associated purely with advection and diffusion.

The physical model is initialized from a resting state, and run with climatological surface and side-boundary forcing for a period of 6 years. The physical state following spin-up is then combined with initial conditions for the ecosystem model to provide complete fields for the coupled physical/ecosystem model. Initial conditions for nitrate, silicate, and phosphorus are taken from the winter season estimates of the 2005 World Ocean Atlas (http://www.nodc.noaa.gov/OC5/WOA05/pubwoa05.html). Initial conditions for all other fields are set to a very small value (10^{-5} μmol P l^{-1} or a related value based on a Redfield ratio). Lateral boundary conditions for the ecosystem components are similar to the initial conditions, except that the nitrate, phosphate and silicate values vary seasonally according to the seasonal average WOA05 fields. The coupled physical/ecosystem model is run with realistic forcing for 6 years duration from 1999 through 2004. The first year, 1999, is considered spin-up of the ecosystem as it adjusts from its initial conditions to a more realistic state and is discarded from our analysis.

3. Results

3.1. Model evaluation

Since the primary aim of this paper is to investigate biodiversity and biogeography in the CCS, it is important to quantitatively evaluate the model performance. In our model, individual phytoplankton analogs with randomly assigned parameters do not exactly correspond to particular, observed phytoplankton species. As a result, we do not focus our model/data evaluation on single phytoplankton analogs, but rather on the total chlorophyll, which we can compare directly to estimates from satellite. Chlorophyll estimates were obtained for years 2000 to 2004 from the monthly Seaviewing Wide Field-of-View Sensor (SeaWiFS) products using the OC4V4 algorithm (O'Reilly et al., 1998) and were provided to us by NOAA Environmental Research Division. Data was reprocessed using a median smoothing algorithm and regridded to the same resolution as the model output.

Fig. 3 shows the 5 year average chlorophyll from (a) the surface level of the numerical model or (b) the satellite derived data. The overall structure of the upwelling system is evident. In both panels, high biomass standing stock is found nearshore, the result of nutrient transport into the photic zone by coastal upwelling. The highest levels found in nature occur in the Gulf of the Farallones (~38°N), north of Cape Mendocino (~41°N), near Heceta Bank (~44°N), and the Washington coast (~46°N). With the exception of the stock off Washington, modeled alongshore chlorophyll variation has a similar alongshore structure though at lower amplitude; small local enhancements to the 5-year average concentration are found in the model output in the Gulf of the Farallones, between Capes Mendocino and Blanco, and a small increase near Heceta Bank. One reason for the reduced amplitude in alongshore chlorophyll variation is the limited representation of nearshore motions due to the model resolution and associated topographic smoothing, common to all terrain-following coordinate models (Haidvogel and Beckman, 1999). In addition, remote sensing observations are biased toward clear days which during upwelling season exhibit higher chlorophyll levels. The high levels observed off Washington and British Columbia have multiple causes, including nutrient supply from the Straits of Juan de Fuca and Columbia river outflows (Hickey and Banas, 2008), neither of which is included in the present model. Noteworthy also in the visual comparison of Fig. 3 is the lower chlorophyll in the southern California Bight. Though the decrease to the south is larger in amplitude than found in nature, the model includes a small phytoplankton increase in the Santa Barbara Channel just south of Pt. Conception as well as a tongue extending to the southeast over the subsurface Santa Rosa Ridge (topographic feature notshown).

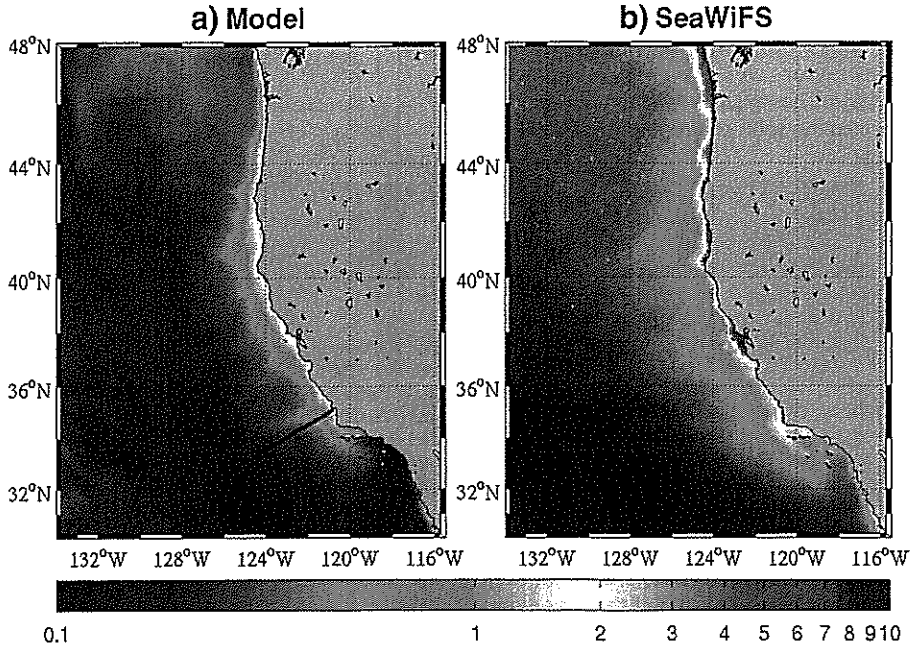

Fig. 3. The five-year average (2000–2004) chlorophyll concentration (mg m^{-3}) from (a) model surface level and (b) SeaWiFS chlorophyll estimate. Model line along CalCOFI Line 77 is displayed in (a).

The cross-shore breadth of the high chlorophyll zone is O (100 km), similar to the observations and other modeling studies (Plattner et al., 2005), though the chlorophyll decrease with distance from coast is somewhat more rapid in the model than in the nature. Offshore levels are consistently low, less than about 0.3 mg chl m^{-3} and consistent with more oligotrophic subtropical gyre water. Modeled chlorophyll is too high in the southwestern portion of the domain, likely the result of a numerical boundary influence.

We quantify model fidelity via a Taylor diagram, which graphically presents the correlation coefficient (CC), standard deviations normalized to that of the observations (NSD), and normalized, centered root mean squared error (RMSE) (Taylor, 2001). In this diagram, radial distance from the origin indicates NSD and the azimuthal direction represents CC, with a maximum of 1 for an angle of 0. Truth in our analysis is defined by the observations and is represented by the point in Fig. 4a labeled SeaWiFS at a value of NSD = CC = 1. The point labeled DOMAIN represents the statistical comparison of panels in Fig. 3 and is found near the intersection of NSD = 0.4 and CC = 0.7. The high value for the correlation coefficient reflects the general agreement in overall structure of the near and offshore fields. To better understand the cause of the roughly one half reduction in variability, we decompose the domain into various subregions, similar to (Gruber et al., 2006). North and South subdomains are divided by latitude 40.5°N, and coastal and offshore regions are delineated by the 1000 m isobath. The overall low standard deviation is dominated by the coastal region and the low-chlorophyll values found nearshore. The southern offshore region has slightly lower NSD than the northern region, both relative to their respective observations, and this low value likely results from the enhanced chlorophyll concentrations modeled in the southwest corner, also discussed above. All subregions exhibit correlation coefficients greater than 0.5. Overall (data minus model) biases are also presented in the diagram as the number in parentheses near each point label. The domain average modeled field has an average bias (B) of -0.13 mg m^{-3}, and this value represents a weighted average of the small value offshore ($B = -0.059$ mg chl m^{-3}) and the considerably larger bias in the coastal zone ($B = -1$ mg chl m^{-3}).

The CCS seasonal cycle is reasonably represented as well (Fig. 4b). Seasons (winter, spring, summer, and fall) are defined as collections of three calendar months (JFM, AMJ, JAS, OND). All seasons have correlation coefficients greater than 0.5, with the largest value (CC = 0.75) occurring in springtime (April–June). Spatial variability in chlorophyll is particularly low (SD ~ 0.2) in Autumn (Oct–Dec) but approximately equal to the 5-year average variability in other seasons. Overall bias is low ($|B| < 0.26$ mg chl m^3) in all seasons with the model usually under-predicting total chlorophyll biomass (i.e., $B < 0$), as in the 5-year average.

3.2. Surface distributions

With good correlation between total phytoplankton chlorophyll modeled and remotely sensed estimates in various parts of the domain, we now investigate the magnitude and distributions of the phytoplankton that make up this total. The 78 independent phytoplankton analogs, initially seeded equally at a low level (10^{-5} μmol $P\,l^{-1}$) and uniformly throughout the domain, self-sort themselves over time into a hierarchy that can be ordered by total biomass contained within the full model volume. The 5-year average field reveals 38 phytoplankton types existing at levels well above the baseline minimum level maintained in the model for all fields. However, most of these members' biomass are extremely small compared to the biomass of the top several contributors. Eight primary producers that have concentrations exceeding 10% of the maximum, and six more maintain biomass between 0.3% and 1% of the maximum. Of these top eight phytoplankton, we find 2 diatoms, 1 LND, 3 PLP, and 2 SNP. In the next grouping of six are 2 diatoms, 2 LND, and 2 PLP. Thus

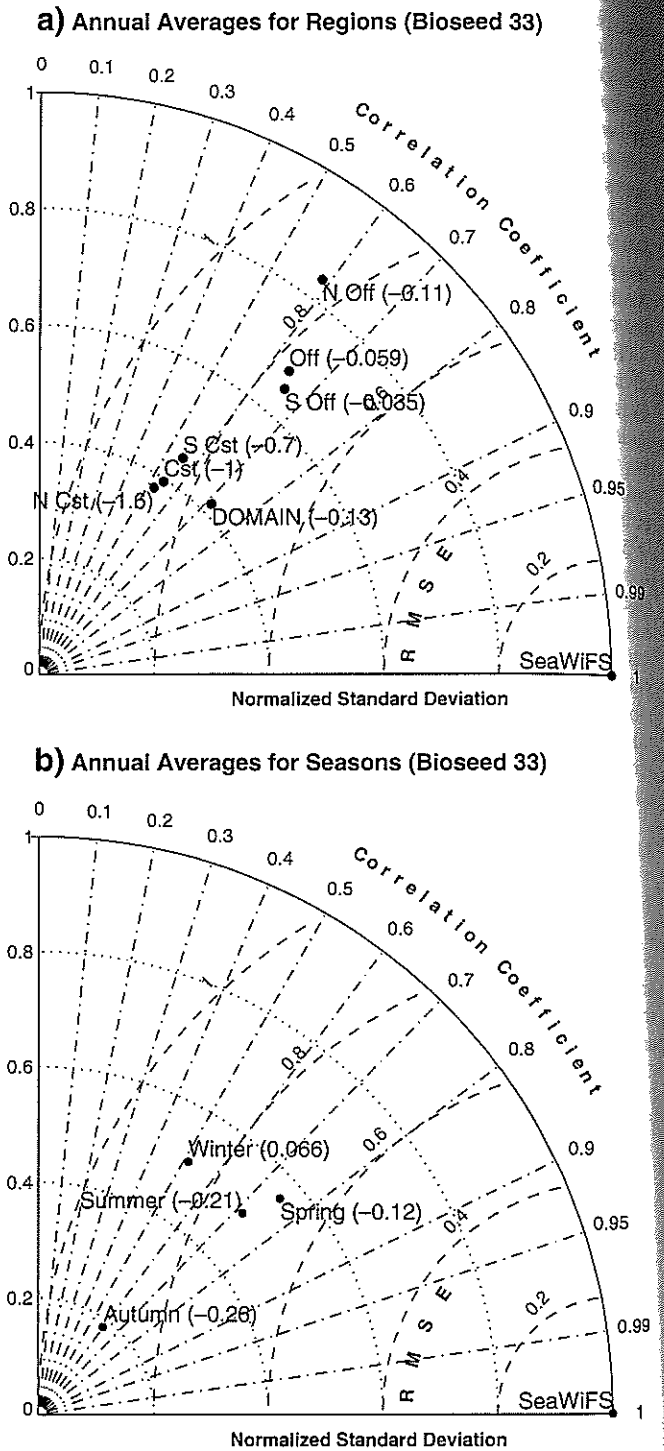

Fig. 4. Taylor diagrams for (a) 5-year average (2000–2004) and (b) seasonal mean chlorophyll concentrations (mg m^{-3}) of model surface level and SeaWiFS observations. In (a) calculations for the entire domain (DOMAIN), coastal and offshore regions (Cst and Off), and Northern and Southern coastal (N Cst and S Cst) and offshore (N Cst and S Cst) regions. North and South regions are divided by latitude 40.5°N, and coastal and offshore regions are on either side of the 1000 m isobath. Bias for each comparison is given in parentheses. In (b), all calculations are for entire domain.

all functional groups enabled are well represented by the model at relatively substantial concentrations, and each consists of further subtypes at various biomass levels. For simplicity, this analysis concentrates on total distributions for each functional group and the top several subtypes.

Geographical distributions illustrate population horizontal structure. Shown in Fig. 5 are the 5-year average surface chlorophyll concentrations for diatoms, PLP, LND, and SNP (note the differing linear color-scale in each panel). In the 5-year average, the total phytoplankton field is dominated numerically by nearshore diatom concentrations. However, at considerably lower but nonzero levels, LND are found more broadly, but at highest concentrations in the coastal transition zone between the upwelling and oligotrophic offshore waters off central California. Also, PLP thrive offshore of the upwelling region, and SNP are distributed throughout the domain, though with largest amplitudes both in the upwelling zone and in more oligotrophic waters offshore.

It is possible to probe further into phytoplankton structure and biogeography by examining the particular subtypes that constitute the functional group totals. Fig. 6 shows the top three PLP and two top SNP organisms in terms of their total biomass. Multiple subtypes are supported within the model, but they are not uniformly distributed. The top three PLP subtypes have different temperature optima (approximately 11°, 17°, and 20 °C), and they thrive in middle, northern, and southern latitudes, respectively. Similarly, the two

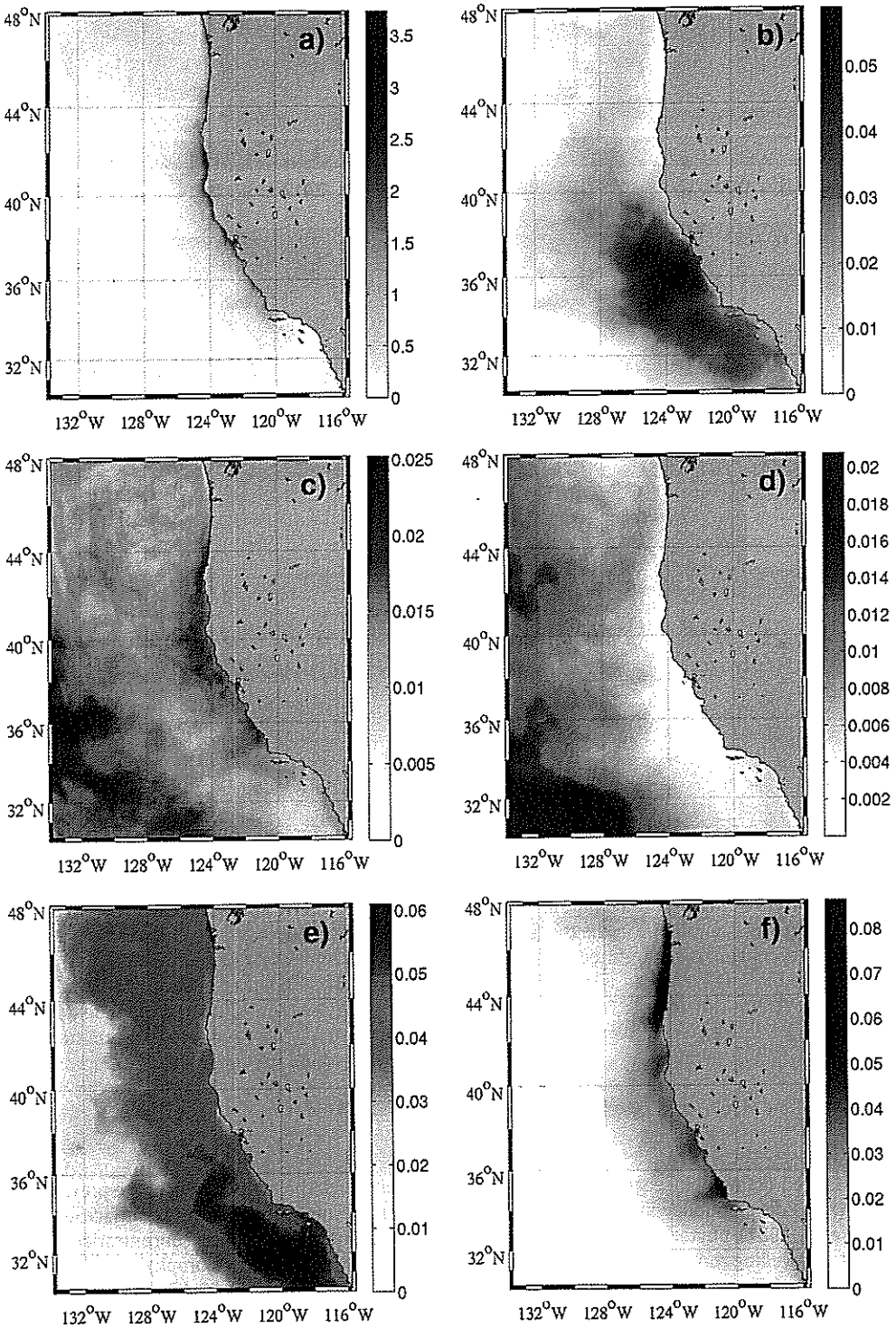

Fig. 5. Five-year average from model surface for (a) diatoms, (b) LND, (c) SNP, (d) PLP, (e) microzooplankton, (f) mesozooplankton. (a–d) show chlorophyll in mg chl m^{-3}), and (e–f) present biomass in terms of μmol P l^{-1}.

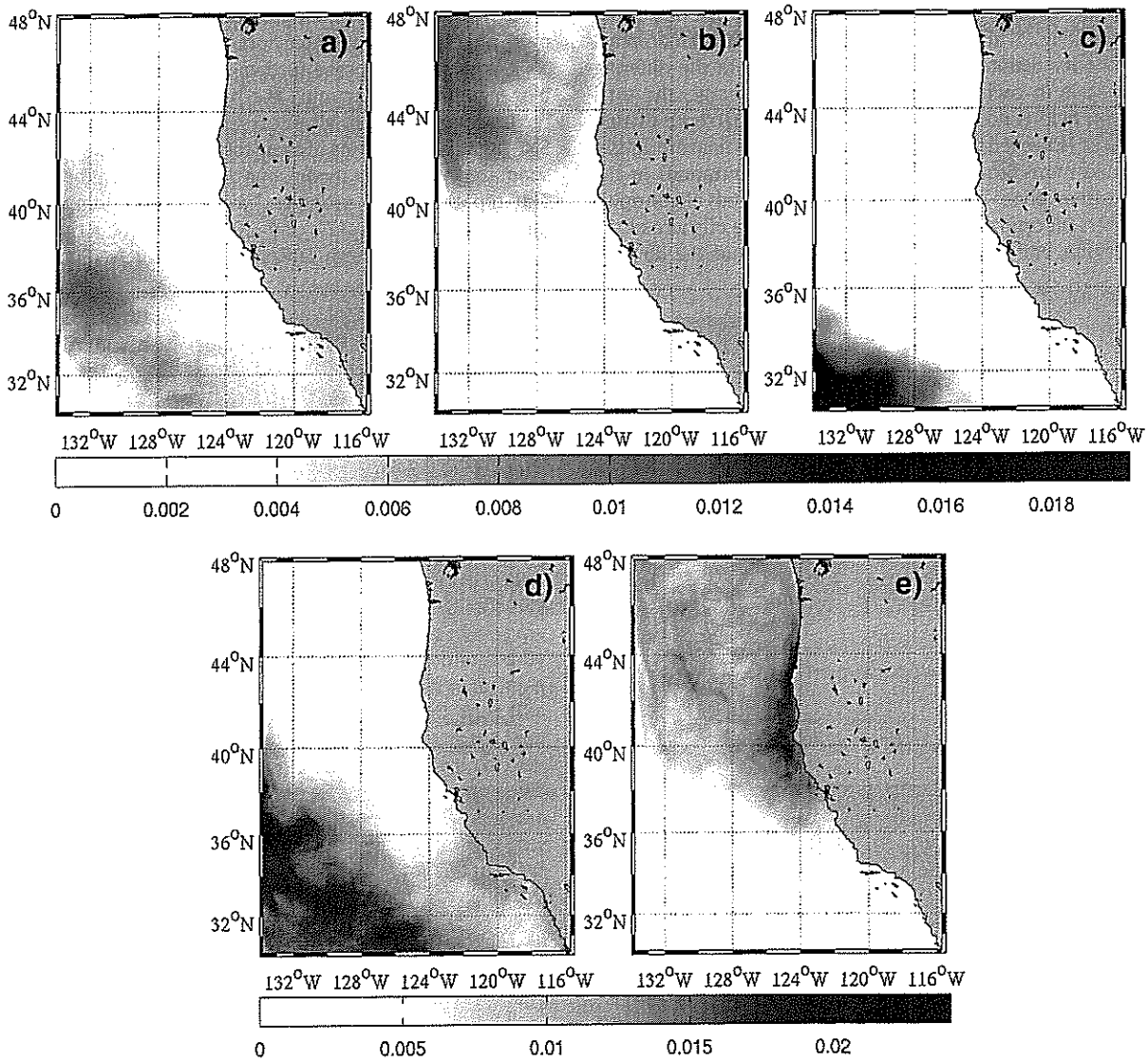

Fig. 6. Five-year average chlorophyll concentration (mg m^{-3}) from model surface for each of the top 3 dominant subgroups for PLP (upper panel: a, b, c) and the top 2 domi subgroups for SNP (lower panel: d, e).

dominant SNP are also distributed according to temperature optima (16° and 10 °C) and are found in the southern and northern portions of the domain.

Surface distributions for grazers in the 5-year average are shown also in Fig. 5. Though found at greatest amplitude in the model in the southern California Bight, microzooplankton distributed over the full extent of the CCS, supported by small and large phytoplankton available for consumption throughout the domain. In contrast, large zooplankton have greatest palatability for large phytoplankton and are found at highest intensity in the upwelling zone, quickly dropping to vanishing levels as offshore distance increases. Grazing of large zooplankton on small zooplankton may also play an important role governing these population distributions.

Over an annual cycle, phytoplankton chlorophyll exhibits a strong seasonal cycle (Fig. 7) with well defined biogeographic patterns. As equatorward alongshore winds develop following the spring transition in March/April (Strub et al., 1987), phytoplankton stocks increase nearshore within the coastal upwelling zone. It is perhaps noteworthy that high coastal biomass is found first to the south along the central and northern California coasts (between Pt. Conception at about 35°N and Cape Mendocino around 40°N), and then to the north along the Oregon and Washington coasts as the upwelling season progresses through August and September. With the weakening of upwell favorable winds in fall (October through Dec), the CCS exhi relatively low phytoplankton levels over much of the domain. Du late winter/early spring (February–April), offshore northern wa undergo an increase in chlorophyll, perhaps due to increa nutrients from wintertime mixing and an increase in solar insolat This broadly distributed offshore stock in the northern CCS is also s in observations (not shown), though in nature it begins in Noven rather than February and at lower amplitude than occurs in the mc The reason for the apparent underproduction offshore in fall overproduction in March is unknown at this time.

3.3. Vertical sections

Although the maps shown in the previous section provide con for organisms that thrive at the surface, additional structure is fo by examining subsurface concentrations. Fig. 8 presents five- average nutrient and chlorophyll sections for both model and along line 77 of the California Cooperative Oceanic Fishe Investigations (www.calcofi.org) which extends offshore from central California coast and is shown in Fig. 3. Nitrate and sili sections in both model and observations show nutrient depletio

Fig. 7. Monthly averages of modeled total chlorophyll concentration (mg chl m^{-3}) at surface.

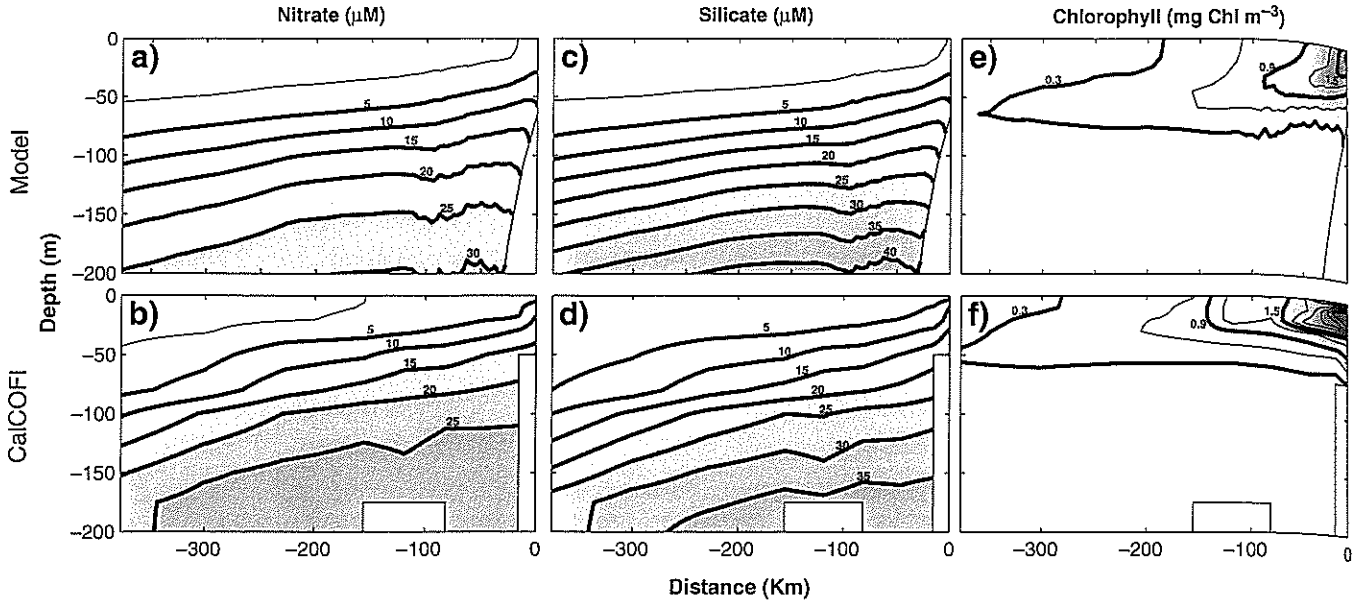

Fig. 8. Five-year average concentrations along line 77 in Fig. 3 in the upper 200 m for the model (a, c, and e) and CalCOFI data (b, d, and f). (a, b) nitrate (μmol N l^{-1}); (c, d) silicate (μmol Si l^{-1}); and (e, f) chlorophyll-a (mg chl m^{-3}). The light contour in panels a, b, c, and d is 1 μmol l^{-1}, and the contour interval in panels e and f is 0.3 mg chl m^{-3}.

the surface with concentrations increasing with depth; a consistent tilt of the isopleths characteristic of a coastal upwelling environment is well represented by the model. In these average sections, modeled surface nutrient values are slightly low relative to the observations. The largest discrepancy occurs in the near to shore, where nutrient isopleths are relatively deep in the model, but rise along the coast in the data. This discrepancy results from either small nutrient upwelling at the coast, overly rapid nutrient drawdown, or some combination. Overall, chlorophyll concentrations also show consistent structure between model and observations. Chlorophyll levels are greatest in the upper 75 m of the water column and increase from low levels offshore to a maximum near shore. The modeled maximum value of approximately 1.9 mg chl m^{-3} is lower than the observed maximum that exceeds 3 mg chl m^{-3}.

The five-year average sections reveal interesting vertical structure in both the model and the data. Near shore, chlorophyll is most concentrated in the upper 25 m, whereas offshore subsurface maxima are found closer to 50 m with particularly low levels above. We explore this structure further by examining particular sections within the CalCOFI collections. Shown in Fig. 9 are modeled chlorophyll (upper panels) and observed values (lower panels) from CalCOFI line 77 during July 2003 and January 2004. For both time-periods, the general structure of the chlorophyll distributions is consistent between observations and model. In wintertime, chlorophyll levels are highest near the surface and decaying with depth. In contrast during summer, a distinct subsurface peak is found offshore near 50 m. The seasonal cycle of the subsurface maximum is shown in monthly averaged sections of modeled chlorophyll (Fig. 10). From November through April phytoplankton structure is characterized by a relatively well-mixed, near surface field, decaying rapidly beneath. In March an upwelling-induced, nearshore bloom at the surface appears, intensifies, and persists through October. From May through October, a broad subsurface chlorophyll maximum develops offshore of the upwelling region. This offshore maximum is found around 60 m depth, at the top of the modeled nutricline and within the thermocline beneath a seasonally warmed surface layer (not shown). Although line 77 presents information less than 400 km from shore, further examination reveals that the subsurface structure is broadly distributed across the CCS (not shown).

Analysis of individual functional group fields indicates that this subsurface chlorophyll maximum, when it occurs, results primarily from diatoms and SNP which exist at much lower levels in the offshore surface waters. The PLP group also contributes to chlorophyll at depth but has significant concentrations above this deep maximum, and therefore this group is not itself responsible for the existence of the subsurface increase. LND are found mostly above the deep maximum. Although the PLP group has a broad presence extending from the surface to the top of the nutricline, subtypes within this group reveal strata. Shown in Fig. 11 are the 5-year averaged July and August fields for the top two PLP. These two subtypes occupy different niches within the water column. PLP #1 ($k_{par}=0.01\ W^{-1}\ m^2$) is adapted to high light conditions and is found near the surface in both months whereas #2 ($k_{par}=0.026\ W^{-1}\ m^2$) is more likely to thrive in subsurface waters with low PAR levels and is found at depth. We note that the subsurface PLP concentrations are exceedingly low and below detection limits for chlorophyll-a and will discuss this aspect and further discuss the subsurface maximum in the Discussion section.

3.4. Temporal cycles

The sequence of plankton populations within the modeled CCS is estimated by integrating the surface biomass distributions horizontally over the domain. Fig. 12 plots time-series for total phytoplankton and individual functional groups. All fields show clear seasonal cycles, but the timing of individual functional group maxima varies. The total phytoplankton field (panel a, blue) reveals a late springtime peak and is dominated by the diatom population (panel b, blue). However, while the diatom population declines to small or near zero levels during fall and winter, the total phytoplankton biomass within the CCS maintains a low level, but well above zero, and evidently supported by non-diatom fields. The small phytoplankton biomass (panel a, green) shows smaller amplitude variation than the total, with maxima in early spring. This more limited seasonal cycle results from two out-of-phase oscillations; SNP (panel c, green) exhibits wintertime increases that precede the growth in and extend longer than the diatom population. In contrast, PLP (panel c, blue) reaches its nadir in spring and maximum in fall. LND (panel b, green) exhibit two peaks annually, with a maximum in the spring but after the diatoms,

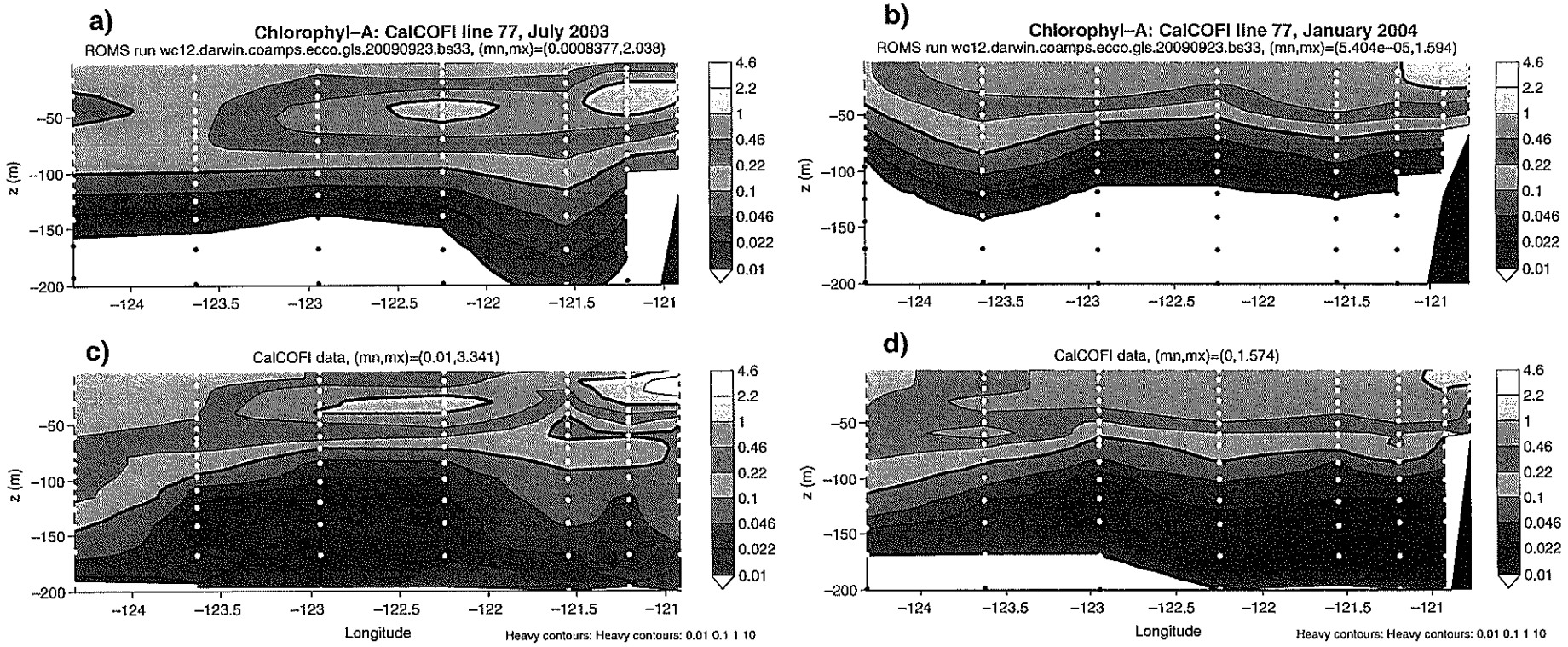

Fig. 9. Instantaneous chlorophyll concentrations (mg chl m^{-3}) along line 77 in Fig. 3 in the upper 200 m for the model (upper panels (a, b)) and CalCOFI data (lower panels (c, d)). July 2003 (left panels (a, c)) and January 2004 (right panels (b, d)).

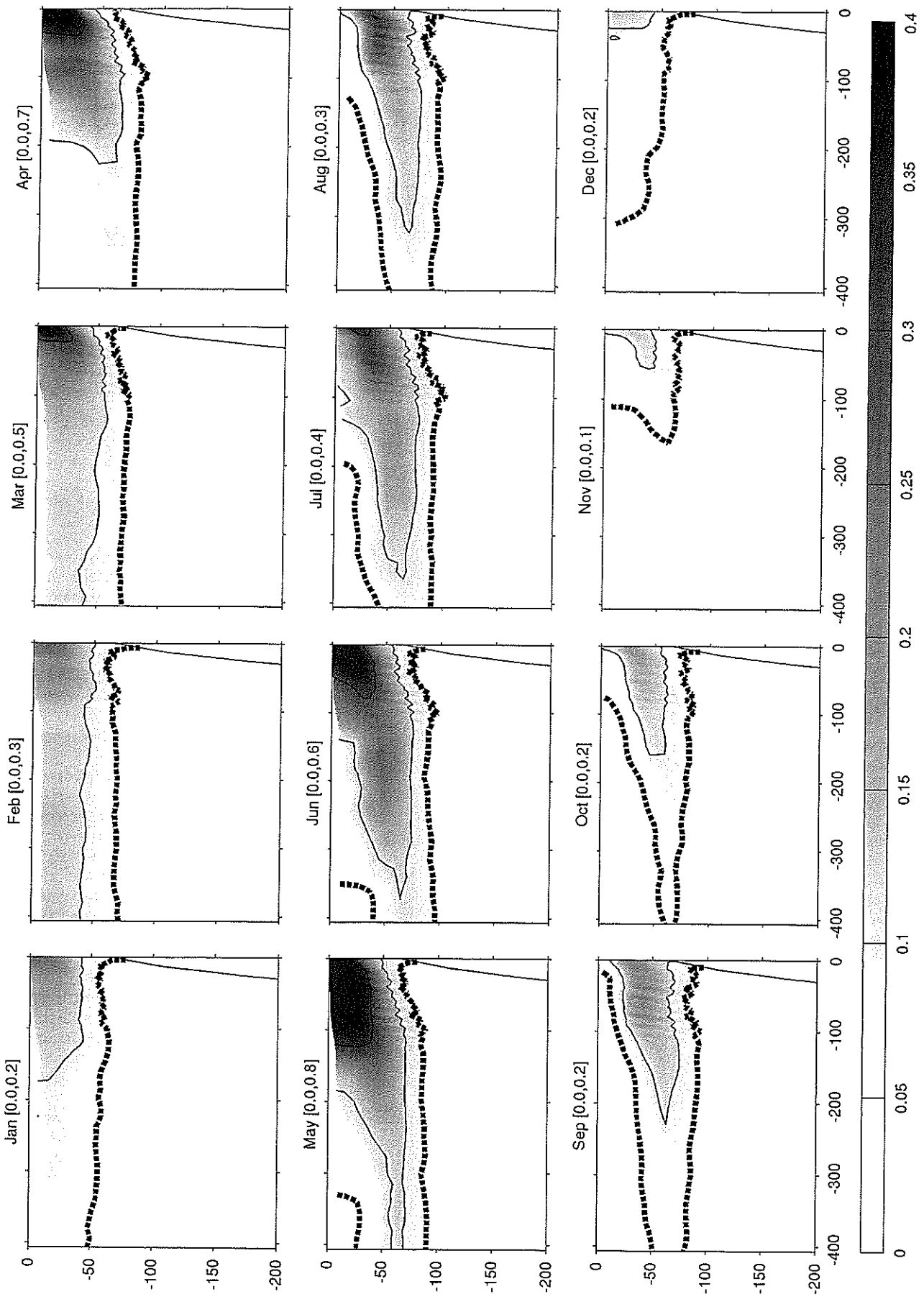

Fig. 10. Monthly averages of modeled total chlorophyll concentration (mg chl m^{-3}) along line 77 in Fig. 3 in the upper 200 m. Monthly minimum and maximum are shown in brackets. *Note that maximum values in a few months exceed the grayscale.* The dashed contour occurs at 0.05 mg m^{-3}. The contour interval for the solid contours is 0.2 mg m^{-3}, beginning at a value of 0.1 m^{-3}.

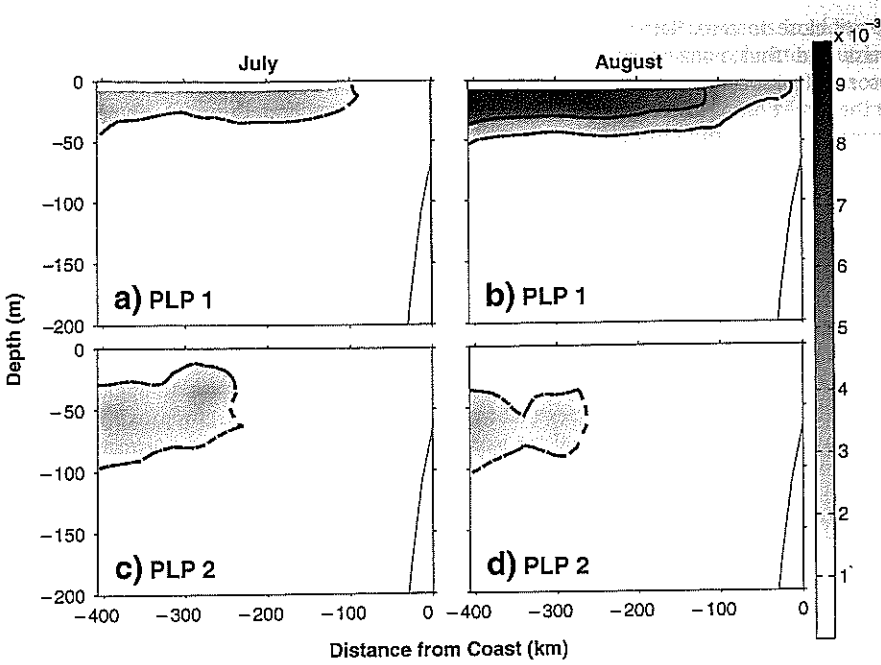

Fig. 11. Monthly averages of modeled chlorophyll concentration along line 77 shown in Fig. 3 for the most abundant (a, b) and second most abundant (c, d) PLP subtypes during the months of July (left column) and August (right column). Dashed contour occurs at 0.001 mg chl m^{-3}. Heavy solid contour levels begin at and occur every 0.005 mg chl m^{-3}. Light solid line at right indicates topography.

and then a subsequent, larger increase in late summer/early fall that is out of phase with the diatom cycle.

For completeness, we present the grazer fields, although given the complex spatial structure of the primary and secondary producers discussed above, we caution about over-interpreting the biomass pathways within the model from this simplistic representation. Like the phytoplankton, the zooplankton fields also display seasonal cycles. Microzooplankton (panel d, blue) levels fluctuate similar to, though slightly later than, the PLP distribution. The microzooplankton fields grow in late summer/autumn, but it is important to note that

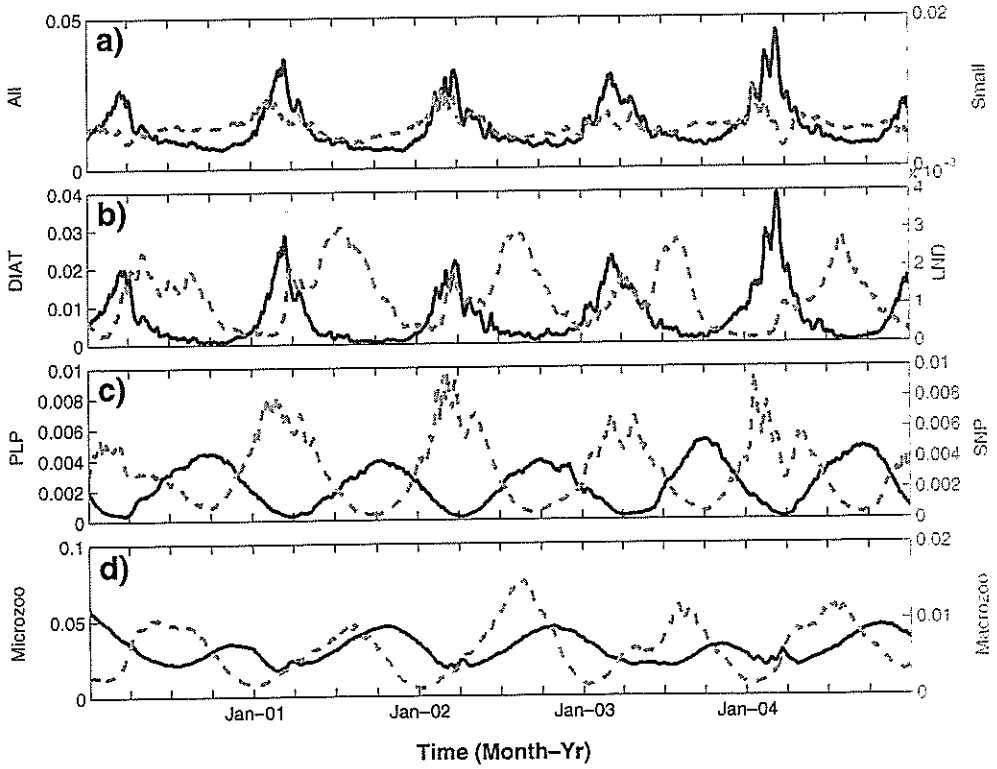

Fig. 12. Time-series of average modeled biomass in near surface waters for (a) total phytoplankton (blue) and small phytoplankton (green), (b) diatoms (blue) and LND (green), (c) PLP (blue) and SNP (green), and (d) microzooplankton (blue) and mesozooplankton (green). All modeled fields are in units of μM P. (For interpretation of the references to color in this figure legend, the reader is referred to the web version of this article.)

Fig. 13. Monthly averages of modeled total chlorophyll concentration (mg chl m^{-3}) along line 77 in Fig. 3 in the upper 200 m. Monthly maximum and minimum are shown in buckets. Note the nonlinear grayscale. The dashed contour occurs at 0.05 mg m^{-3}. The contour interval for the solid contours is 0.2 mg m^{-3}, beginning at a value of 0.1 m^{-3}.

their minimum levels are not close to zero. Rather, they sustain a nonzero integrated biomass and thus nonzero grazing pressure throughout the year. Mesozooplankton (panel d, green) begin to develop early in the year at the same time as diatoms, but it reaches its maxima well after the diatom peak, near the same time as the LND group. The large zooplankton approaches very small levels in winter, unlike the offseason for small grazers.

As with the surface maps, each functional group can be further inspected for subtypes. Fig. 13 shows the top few subtypes for diatoms, LND, SNP, and PLP in panels a, b, c, and d, respectively. Whereas big phytoplankton groups are dominated by single subtypes, the small phytoplankton can be divided into multiple non-negligible components whose timing for growth and decline are shifted and apparently unrelated. It is perhaps surprising that the spring and fall increases in LND result from only one subtype, but it argues that for some organisms, environmental conditions for which they are best adapted can arise at multiple times in the year, and not simply once in an annual cycle.

4. Discussion

The goal of this study is to evaluate the emergent community ecosystem model for its capacity to represent the biodiversity and biogeography of the California Current System. Observations have long shown diverse, heterogeneous planktonic communities, though usually with single or a few species numerically dominant. Studies based on phytoplankton counts focused on larger taxa. The Balech (1960) study of coastal waters off Scripps pier in Southern California documented both diatoms and dinoflagellates, with diatoms being most abundant but dinoflagellates comprising half the listed phytoplankton. Bolin and Abbott (1963) reported that while one genus (*Chaetoceros* spp.) appeared most numerous in the large-sized phytoplankton population in Monterey Bay between 1954 and 1960, 17 other genera were observed at lower levels. More broadly, Venrick (2009) identified 294 taxa of phytoplankton along Line 87 from the CalCOFI sampling grid off southern California. The most abundant were a centric diatom (*Chaetoceros debilis*), a coccolit phorid (*Emilinia huxleyi*) and a pennate diatom (robust *Pseu nitzschia*). Together, these three species accounted for 61% of the t abundance, and thus the numerical contribution of most of remaining 291 taxa to the total is extremely small. More mod techniques have revealed extensive picophytoplankton abunda further contributing to this biodiversity. Flow cytometer analysis epifluorescence microscopy have documented the presence *Synechococcus* and picoeukaryotes, and to a lesser extent *Proch ococcus*, in different coastal domains off Oregon and California (H et al., 1991; Collier and Palenik, 2003; Worden et al., 2004; Sherr et 2005).

Overall, the model output analyzed in this manuscript represe this observed phytoplankton biodiversity. Of 78 phytoplankton ty seeded in the model, approximately 40 coexist in the multi-y average. The top 14 organisms in terms of area averaged surf biomass span 3 orders of magnitude in that measure; they incluc diatoms, 3 large non-diatoms (a group which would incl dinoflagellates), 5 *Prochlorococcus*-like organisms, and 2 sn phytoplankton that can use nitrate (which would incl *Synechococcus* and picoeukaryotes). Although the breadth of org isms and functional groups is not as extensive as that in nature represents a significant advance over existing ecosystem models t characterize the phytoplankton community with only one or t components.

The model biogeography also shows considerable promise wl compared to observations. We quantitatively evaluated the t modeled chlorophyll against SeaWiFS-derived surface chloropl estimates on a 5-year and seasonal mean basis. The model shows g representation of the general pattern of standing stock in California Current System (0.5<CC<0.75) for the years 2000–2C The standard deviation of total chlorophyll is approximately one l that observed in nature. In part we believe, this low variability res from limited (~10 km) physical model resolution, and though shown in this paper, this measure can be adjusted also through so parameter tuning, such as of the carbon to chlorophyll ra

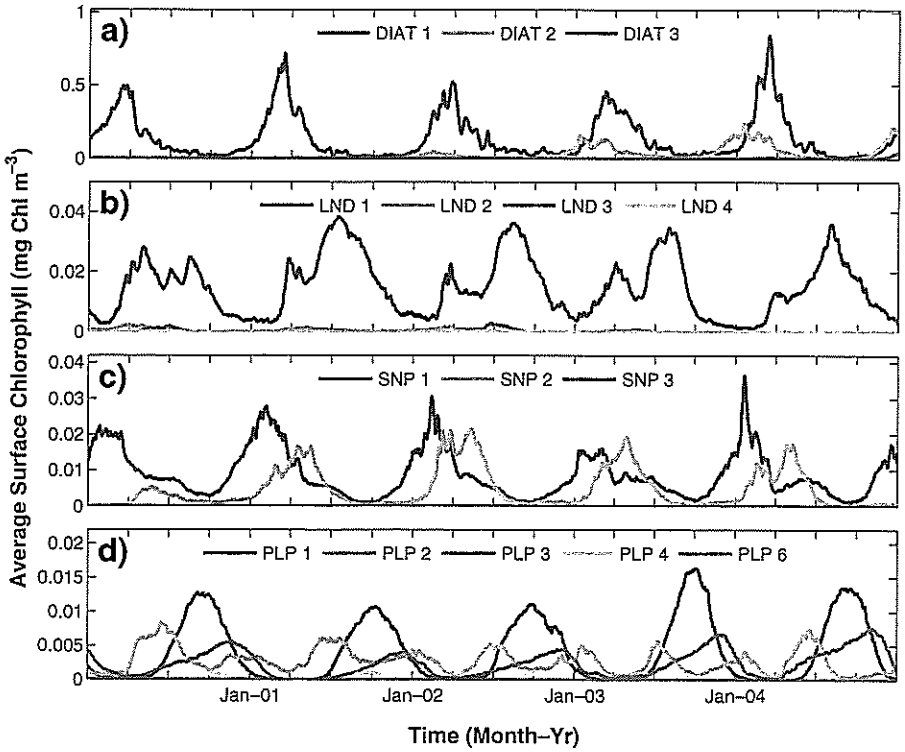

Fig. 13. Time-series of average modeled biomass in near surface waters for the most abundant (a) diatoms, (b) LND, (c) SNP, and (d) PLP subtypes. Biomass units are mg chl m

Noteworthy peaks and deficits of surface chlorophyll are found along the coast at multiple locations in both model and observations. The most widely-recognized biogeographic boundary in the California Current System occurs in nature at Pt. Conception (Checkley and Barth, 2009). In our model, this break is visible in both the total surface phytoplankton stock (Fig. 3) and in the surface diatom field (Fig. 5a). It is perhaps a failing of the model that this break is not clearly visible at the next higher trophic level (Fig. 5e and f). However, our effort has focused on phytoplankton diversity, and it may be that greater resolution of the zooplankton community and/or explicit temperature dependence of grazing or metabolic rate may be necessary.

The general horizontal structure of the modeled functional groups also appears reasonable, though our ability to quantitatively evaluate this aspect is not as great as with the total phytoplankton stock. It is well known that high nutrient input resulting from coastal upwelling in the CCS drives new production of nearshore diatom blooms (Barber and Smith, 1981), with considerably smaller diatom abundance found in oligotrophic waters. The cross-shore diatom structure is common to other, single functional group models (e.g., Gruber et al., 2006) and also idealized studies (Edwards et al., 2000a; Spitz et al., 2003). Less common is the representation of *Prochlorococcus* (our PLP group) and *Synechococcus* or picoeukaryotes (our SNP group). In our multi-year average, we find an increase in our SNP group close to the coast and offshore, with a smaller but still significant presence all through the domain. PLP shows a distinct deficit in the nearshore upwelling zone with increasing concentration westward and to the south in more oligotrophic waters (Fig. 5).

We believe that this structure in the small phytoplankton is consistent with observations. Worden et al. (2004) found off the Scripps pier in southern California that *Synechococcus* dominated cell abundance and picoeukaryotes contributed most to estimated carbon biomass. Along a transect off Oregon, Sherr et al. (2005) found small-sized phytoplankton dominated by *Synechococcus* and picoeukaryotes at near shore stations just offshore of the upwelling front. Collier and Palenik (2003) identified a gradient in *Synechococcus* abundance across the CalCOFI sampling grid, with highest levels nearshore of the California Current and lower levels offshore. *Prochlorococcus* shows the opposite tendency. Worden et al. (2004) report that *Prochlorococcus* were small contributors to total biomass and sometimes not found at all at their coastal station. Sherr et al. (2005) observed *Prochlorococcus* only at one offshore station in their sampling grid. In contrast, at Station ALOHA in the North Pacific Subtropical Gyre, *Prochlorococcus* has been found to contribute about 40% or more of the total photosynthetic biomass (Campbell et al., 1994).

Another aspect of the CCS biogeography that the model represents is the subsurface chlorophyll maximum. This feature has a long history of observations in the California Current System (Anderson, 1969; Cullen and Eppley, 1981; Cullen et al., 1982). Venrick et al. (1973) described its broad structure across the Pacific Ocean (and in the CCS) and noted how it can develop seasonally in summer with increased water column stability. In our model, a broadly distributed subsurface chlorophyll maximum is found offshore from about May to October. We presented instantaneous and averaged sections along CalCOFI line 77. In terms of chlorophyll amplitude and approximate depth range, this feature bears quantitative similarity to observations. However, it is not obvious that this structure is maintained by the same processes as that in nature. Several mechanisms (e.g., local production, sinking convergence, grazing, and photo-acclimation) have been proposed to explain the existence of the maximum. Using traditional fluorescence measurements and microscopy, Venrick et al. (1973) associated this feature with unique diatom assemblages, increased phytoplankton cell numbers, and possibly increased chlorophyll per cell. Recently, Fennel and Boss (2003) argued that in various oligotrophic systems the subsurface chlorophyll maximum as estimated by fluorescence is deeper than and physically separated from phytoplankton biomass maximum as approximated by beam attenuation measurements. In addition, they used a 1-dimensional, steady-state model of phytoplankton, nutrient, and chlorophyll to show that the subsurface biomass maximum occurs at the depth where production and losses balance, whereas the deeper chlorophyll maximum results from photo-acclimation.

Our model has the potential to exhibit a photo-acclimation induced peak through the selection of organisms with high chlorophyll to carbon ratios (e.g., low-light adapted *Prochlorococcus*-like organisms and small non-*Prochlorococcus*). Model output does show vertical structure in the vertical within the *Prochlorococcus*-like organisms. Highest total concentrations are found at the surface, though subtypes with low-light adaptations occupy subsurface strata. These broad descriptions are similar to those outlined from observations along the Atlantic Meridional Transect by Johnson et al. (2006) and have been observed and modeled at Station ALOHA (Rabouille et al., 2007). But our modeled concentrations are much lower than observed. Rather, we find this maximum is dominated by diatoms and SNP. The high diatom concentration suggests that our chlorophyll maximum results at least in part from high phytoplankton biomass, more consistent with the observations of Venrick et al. (1973) and less so with those of Fennel and Boss (2003). One limitation in our model is the constant carbon to chlorophyll ratio for each phytoplankton functional group. It is likely that a variable carbon to chlorophyll model, such as Geider et al. (1996), would enable a more complex and realistic representation of this subsurface phytoplankton community and chlorophyll structure.

Finally, we have investigated the annual cycle of area averaged phytoplankton functional groups in the CCS. Garrison (1979) observed communities in Monterey Bay in which diatoms dominated from winter through the upwelling period and dinoflagellates occasionally became more abundant in the fall. Chavez et al. (2002) suggest that nearshore central California coastal waters transition from a diatom dominated upwelling system to a picoplankton community in the so-called oceanic (fall) period. We find diatoms exhibit the largest chlorophyll concentrations in the multi-year average, but that their amplitudes are highly variable in time. Highest diatom chlorophyll concentrations occur in the spring/summer period (Fig. 13), and large phytoplankton that do not require silicate peaks in late summer/early fall during the diatom minimum. Small phytoplankton also experience strong seasonal cycles, with our PLP and SNP largely out of phase with one another; we find a fall peak and a spring minimum in *Prochlorococcus*-like organisms.

The results presented in this paper describe only one realization of this ecosystem model. One distinguishing feature of the present approach is the method of parameter selection. Although, as in more traditional models, many important constants in this model are chosen by the operator, a few key parameters that govern phytoplankton growth are selected randomly within reasonable ranges. Different realizations of the random numbers will yield different subsets of virtual phytoplankton, allowing for potentially very different autotrophic communities. While our main realization described in this manuscript consists of 5 years of model output, we have also investigated other randomizations for a shorter duration. Fig. 14 presents the Taylor diagram comparing total phytoplankton at the surface from 5 ecosystem realizations to SeaWiFS chlorophyll estimates for the year 2000 (one year following ecosystem spinup). Number 1 corresponds to the run described throughout this paper. It is evident that all ecosystem realizations have similar domain-wide correlation coefficients ($0.6<CC<0.7$). Greater scatter is found in the radial direction, and run 3 has the largest NSD, and the point closest to the SeaWiFS estimate. All runs also have very similar biases. Thus changing the modeled phytoplankton through random physiological responses gives very robust model output in terms of total, averaged phytoplankton biomass.

What does vary in different realizations is the underlying number and detailed distribution of significant functional group subtypes that

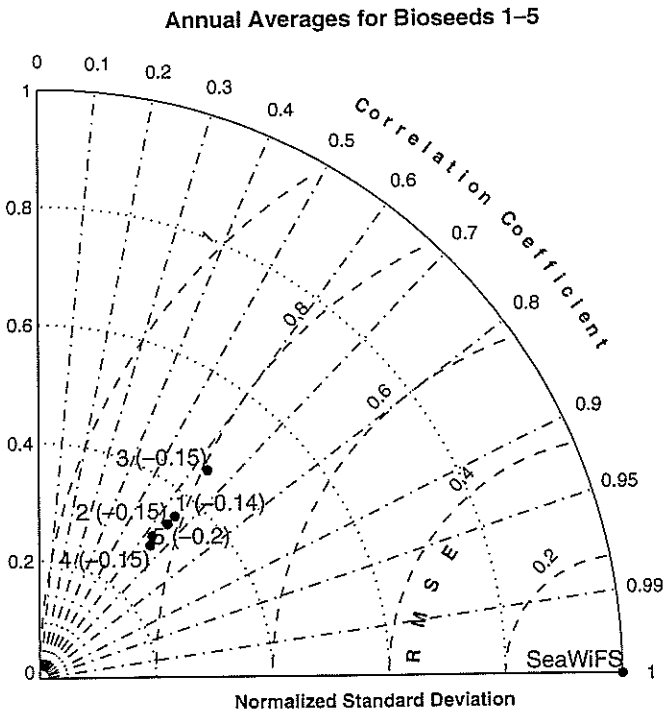

Fig. 14. Taylor diagram for the year 2000 annual mean chlorophyll concentration (mg m^{-3}) in near surface waters of model output and SeaWiFS observations across five randomized runs. Run 1 is that used throughout the manuscript. The bias for each comparison is given in parentheses.

emerge. Within each realization, all four functional groups have members that exist at levels exceeding 10% of the maximum biomass. Most consistent among realizations is (a) the existence of one, two, or three coastal diatoms of significant biomass, (b) the offshore presence of PLP, and (c) the occurrence of SNP both on and offshore. LND are the most variable functional group across realizations, with representatives that inhabit the coastal transition zone/offshore regions (runs 2 and 4), the coastal domain (run 3) or both (runs 1 and 5).

Our effort raises the question as to whether one requires dozens of phytoplankton species to model the California Current Ecosystem accurately, and the answer is clearly problem-specific (or metric-specific). Simpler models (e.g., Gruber et al., 2006) can do an excellent job of approximating total chlorophyll, for example, and are considerably less costly in terms of required computer resources. But by construction, they are more limited in resolving independent phytoplankton populations and some biological pathways that are part of the natural ecosystem. Biogeographic breaks of sub-populations also require more biodiversity than just a few phytoplankton species can provide. Lastly, community shifts that derive from modeled environmental changes can be represented in a phytoplankton rich structure such as this one.

We note that all ecosystem models are limited in their representation of particular biological processes and here we mention a few shortcomings of the present model. Large non-diatoms are a group defined in this model that, within the California Current System, arguably represents flagellates and dinoflagellates. Evidence supports these organisms attaining resources in more complex ways than typical of other phytoplankton, such as through mixotrophy, vertical migration, and assimilation of nitrogen in the dark (Harrison, 1976), which are not included in the model. Although zooplankton populations have been shown to play a large role in shaping the structure of the phytoplankton community (Verity and Smetacek, 1996), and species-specific preferences of zooplankton on phytoplankton have been reported (e.g., Cowles et al., 1988; Flynn et al., 1996), we implemented a relatively simple zooplankton representation with only one large and one small member. While Redfield ratios enable a compact representation that is computationally efficient for ecosystem models, considerable evidence reveals interesting deviations from these quantities under periods of nutrient stress (Geider and La Roche, 2002). In the present model, phytoplankton are assumed to be in Redfield proportions. Quantitative model evaluation was aided by variable, group-specific carbon to chlorophyll ratio. Above, we noted the potential for a variable carbon to chlorophyll model to improve the representation of the subsurface chlorophyll structure. Finally, we have neglected the influence of iron as a limiting micronutrient in the model. Evidence (e.g., (Hutchins and Bruland, 1998; Bruland et al., 2001) has shown the possibility for iron limitation within the coastal waters of the California Current System, and this model capability remains to be explored.

Thus, the neglect of some phytoplankton behavior, lack of mixotrophy, limited grazer diversity, assumed Redfield stoichiometry for phytoplankton, fixed carbon to chlorophyll ratios, and the omission of iron as a limiting resource are all aspects of the model that could be improved upon. However, despite these shortcomings, this model does an excellent job of representing many aspects of the California Current Ecosystem and offers for the first time in this region substantial biodiversity of modeled organisms with temporal and spatial structure that should further illuminate role of physical and biological processes that govern these populations.

Acknowledgements

We are grateful to the Gordon and Betty Moore Foundation for grants supporting this research. Thanks to Jim Doyle for help with COAMPS and to Patrick Heimbach for assistance with the ECCO product. The work was aided by valuable conversations with Jerome Fiechter, Andy Leising, Sophie Rabouille, Francisco Chavez, and Stephanie Dutkiewicz, and the comments of two reviewers improved the manuscript. SeaWiFS data provided by NOAA, Pacific Fisheries Environmental Laboratory, courtesy of NASA Goddard Space Flight Center, Ocean Biology Products Group and Geoeye, Inc.

Appendix A

This appendix documents the equations used in the ecosystem model, shown schematically in Fig. 1. Constants used in the formulation are given in Tables A.1, A.2, and A.3. Using words to represent processes, the rates of change of model state variables can be expressed

$$\frac{\partial \text{ phytoplankton}}{\partial t} = \textit{uptake} - \textit{grazing} - \textit{phytoplankton mortality}$$

$$\frac{\partial \text{ zooplankton}}{\partial t} = \textit{assimilated grazing} - \textit{zooplankton mortality}$$

$$\frac{\partial \text{ nutrients}}{\partial t} = \textit{remineralization} - \textit{uptake}$$

$$\frac{\partial \text{ particulates}}{\partial t} = \textit{export to particulates} - \textit{particulate remineralization} - \textit{sinkin}$$

$$\frac{\partial \text{ dissolved organics}}{\partial t} = \textit{export to dissolved} - \textit{dissolved remineralizat}$$

where the word *export* refers to the transfer of material to particula or dissolved pools via phytoplankton mortality, zooplankton mort ity, and unassimilated grazing. The *particulate* pool refers to no living, particulate matter.

It is convenient to describe each process individually and consic separately the associated rate of change for each state variable. T model includes N_p phytoplankton members and N_z zooplankt

organisms. We use subscripts, i, j, and k to identify individual phytoplankton or zooplankton but omit these indices when the context is clear. All state variables, which are concentrations and denoted with square brackets, are functions of space and time, (e.g.,

$$[P_i] = [P_i](x,y,z,t) \tag{A.1}$$

for phytoplankton i) though we omit reference to these dependencies except when necessary for clarity.

For each phytoplankton, i, growth by nutrient uptake is given by

$$U_i = \mu_i I_{lim} N_{lim} T_{lim} [P_i] \tag{A.2}$$

where μ_i is the maximum growth rate. Growth is reduced from its maximum value by three factors, I_{lim}, N_{lim}, and T_{lim}, representing limitation by light, nutrients, and temperature, respectively.

The light function is expressed

$$I_{\text{lim}} = \frac{1}{\gamma}\left(1 - e^{-k_{\text{par}} I_{\text{PAR}}}\right) e^{-k_{\text{inh}} I_{\text{PAR}}} \tag{A.3}$$

$$\gamma = \frac{k_{\text{par}}}{k_{\text{par}} + k_{\text{inh}}} e^{\frac{k_{\text{inh}}}{k_{\text{par}}} \ln\left(\frac{k_{\text{inh}}}{k_{\text{par}} + k_{\text{inh}}}\right)}. \tag{A.4}$$

Here, I_{PAR} is the local photosynthetically active radiation, which depends on the surface PAR, I_s, and subsurface total phytoplankton concentration:

$$I_{\text{PAR}}(z) = I_s e^{-\int_z^0 (k_0 + k_p P_T(z))dz} \tag{A.5}$$

and

$$P_T(z) = \sum_{i=0}^{N_p} [P_i](z). \tag{A.6}$$

Parameters k_{inh} and k_{par} are phytoplankton-dependent,

$$k_{\text{par}} = |\mathcal{N}\left(\overline{k_{\text{par}}}, \sigma_{k_{\text{par}}}\right)| \tag{A.7}$$

$$k_{\text{inh}} = |\mathcal{N}\left(\overline{k_{\text{inh}}}, \sigma_{k_{\text{inh}}}\right)| \tag{A.8}$$

where $\mathcal{N}(\bar{\nu}, \sigma_\nu)$ is a normal random deviate with mean, $\bar{\nu}$, and standard deviation, σ_ν. Values for the means and standard deviations of these light parameters are provided in Table A.1.

Limitation by temperature, T, is given by

$$T_{\text{lim}} = c_a \left(c_b^T e^{-\left(\frac{|T - T_0|}{T_d}\right)^\tau} - T_n \right) \tag{A.9}$$

where

$$T_0 = \mathcal{U}(T_{\min}, T_{\max}) \tag{A.10}$$

is the temperature optimum, and $\mathcal{U}(\nu_0, \nu_1)$ is a uniform random deviate between ν_0 and ν_1.

Nutrient limitation is determined as the minimum of multiple nutrient limitation functions, the choice of which depends on the silicate requirement and the forms of nitrogen utilized. For phytoplankton that require silicate and process all three forms of nitrogen,

$$L_P = \frac{[PO_4]}{k_{PO4} + [PO_4]} \tag{A.11}$$

$$L_{\text{Si}} = \frac{[\text{Si(OH)}_4]}{k_{\text{Si}} + [\text{Si(OH)}_4]} \tag{A.12}$$

$$L_{\text{NH}_4} = \frac{[\text{NH}_4]}{k_{\text{NH}_4} + [\text{NH}_4]} \tag{A.13}$$

$$L_{\text{NO}_2} = \frac{[\text{NO}_2]}{k_{\text{NO}_3} + [\text{NO}_2] + [\text{NO}_3]} e^{-\sigma_\lambda [\text{NH}_4]} \tag{A.14}$$

$$L_{\text{NO}_3} = \frac{[\text{NO}_3]}{k_{\text{NO}_3} + [\text{NO}_2] + [\text{NO}_3]} e^{-\sigma_\lambda ([\text{NH}_4])} \tag{A.15}$$

$$L_N = L_{\text{NH}_4} + L_{\text{NO}_2} + L_{\text{NO}_3}. \tag{A.16}$$

For phytoplankton that do not use silicate but assimilate ammonium and nitrite, we set

$$L_P = \frac{[PO_4]}{k_{PO_4} + [PO_4]} \tag{A.17}$$

$$L_{\text{NH}_4} = \frac{[\text{NH}_4]}{k_{\text{NH}_4} + [\text{NH}_4]} \tag{A.18}$$

$$L_{\text{NO}_2} = \frac{[\text{NO}_2]}{k_{\text{NO}_2} + [\text{NO}_2]} e^{-\sigma_\lambda [\text{NH}_4]} \tag{A.19}$$

$$L_N = L_{\text{NH}_4} + L_{\text{NO}_2}. \tag{A.20}$$

For autotrophs that do not use silicate and take up ammonium only,

$$L_P = \frac{[PO_4]}{k_{PO_4} + [PO_4]} \tag{A.21}$$

$$L_{NH4} = \frac{[NH_4]}{k_{NH4} + [NH_4]} \tag{A.22}$$

$$L_N = L_{NH4}. \tag{A.23}$$

Half saturation constants for nutrient uptake are assigned as uniform random deviates between bounds given in Table A.1. Finally, the nutrient limitation factor is defined

$$N_{\text{lim}} = \begin{cases} \min(L_P, L_{Si}, L_N) & \text{diatom} \\ \min(L_P, L_N) & \text{otherwise} \end{cases}. \tag{A.24}$$

The rate of change of phytoplankton biomass and nutrients due to growth by a single phytoplankter is expressed

$$\frac{\partial [P_i]}{\partial t} = U_i \tag{A.25}$$

$$\frac{\partial [PO_4]}{\partial t} = -U_i \tag{A.26}$$

$$\frac{\partial [Si(OH)_4]}{\partial t} = \delta_{Si} r_{SiP} \frac{\partial [PO_4]}{\partial t} \tag{A.27}$$

$$\frac{\partial [NO_3]}{\partial t} = f_{NO3} r_{NP} \frac{\partial [PO_4]}{\partial t} \tag{A.28}$$

$$\frac{\partial [NO_2]}{\partial t} = f_{NO2} r_{NP} \frac{\partial [PO_4]}{\partial t} \tag{A.29}$$

$$\frac{\partial [NH_4]}{\partial t} = f_{NH4} r_{NP} \frac{\partial [PO_4]}{\partial t}. \tag{A.30}$$

in which the variable δ_{Si} takes on a value of 1 if silica is required and 0 when it is not, and factors r_{SiP}, etc., are Redfield ratios. Using the δ notation also for nitrogen utilization, we define the factors that partition nitrogen uptake to depend on both this ability to use a particular form and the relative availability of that resource:

$$f_{NO3} = \delta_{NO3}\frac{L_{NO3}}{L_N} \tag{A.31}$$

$$f_{NO2} = \delta_{NO2}\frac{L_{NO2}}{L_N} \tag{A.32}$$

$$f_{NH4} = \delta_{NH4}\frac{L_{NH4}}{L_N}. \tag{A.33}$$

For grazing, we consider processes influenced by zooplankton k. Total grazable material for zooplankton k, weighted by its palatability, is given by

$$A_k = \sum_{i=0}^{N_p} \pi_{ki}^{(P)}[P_i] + \sum_{j=1}^{N_z} \pi_{kj}^{(Z)}\left[Z_j\right] \tag{A.34}$$

where $\pi_{ki}^{(P)}$ and $\pi_{kj}^{(Z)}$ represent the palatability of phytoplankton i and zooplankton j for grazer k. The rate for grazing of zooplankton j by zooplankton k is given by

$$G_{kj}^{(Z)} = \frac{G_k^{\max}\pi_{kj}^{(Z)}\left[Z_j\right]A_k}{k_g^2 + A_k^2} \tag{A.35}$$

which then gives the rates of change for zooplankton biomass and particulate and dissolved concentrations by grazing of organism j by k:

$$\frac{\partial\left[Z_j\right]}{\partial t} = -G_{kj}^{(Z)}[Z_k] \tag{A.36}$$

$$\frac{\partial[Z_k]}{\partial t} = \alpha_k^{(Z)}G_{kj}^{(Z)}[Z_k] \tag{A.37}$$

$$\frac{\partial[POP]}{\partial t} = E^{(G)}\left(1-\alpha_k^{(Z)}\right)G_{kj}^{(Z)}[Z_k] \tag{A.38}$$

$$\frac{\partial[DOP]}{\partial t} = \left(1-E^{(G)}\right)\left(1-\alpha_k^{(Z)}\right)G_{kj}^{(Z)}[Z_k]. \tag{A.39}$$

The parameters $\alpha^{(Z)}$ and $E^{(G)}$ represent the assimilation efficiency and fraction exported to particulate matter, respectively.

Analogously, the grazing rate for zooplankton k on phytoplankton i is given by

$$G_{ki}^{(P)} = \frac{G_k^{\max}\pi_{ki}^{(P)}[P_i]A_k}{k_g^2 + A_k^2} \tag{A.40}$$

which yields for each component

$$\frac{\partial[P_i]}{\partial t} = -G_{ki}^{(P)}[Z_k] \tag{A.41}$$

$$\frac{\partial[Z_k]}{\partial t} = \alpha_k^{(P)}G_{ki}^{(P)}[Z_k] \tag{A.42}$$

$$\frac{\partial[POP]}{\partial t} = E^{(G)}\left(1-\alpha_k^{(P)}\right)G_{ki}^{(P)}[Z_k] \tag{A.43}$$

$$\frac{\partial[DOP]}{\partial t} = \left(1-E^{(G)}\right)\left(1-\alpha_k^{(P)}\right)G_{ki}^{(P)}[Z_k]. \tag{A.44}$$

While phosphorus is the sole currency for phytoplankton with stoichiometry fixed according to Redfield ratios, separate silica, nitrogen and phosphorus budgets are maintained for zooplankton. As a result, zooplankton stoichiometry can vary; the Si:N and Si:P ratios can change depending on the fraction of diatoms consumed.

Mortality of phytoplankton and zooplankton induce changes in biomass and dissolved and particulate compartments,

$$\frac{\partial[P_i]}{\partial t} = -m^{(P)}[P_i] \tag{A.45}$$

$$\frac{\partial\left[Z_j\right]}{\partial t} = -m^{(Z)}\left[Z_j\right] \tag{A.46}$$

$$\frac{\partial[POP]}{\partial t} = E^{(P)}m^{(P)}[P_i] + E^{(Z)}m^{(Z)}\left[Z_j\right] \tag{A.47}$$

$$\frac{\partial[DOP]}{\partial t} = \left(1-E^{(P)}\right)m^{(P)}[P_i] + \left(1-E^{(Z)}\right)m^{(Z)}\left[Z_j\right]. \tag{A.48}$$

Remineralization processes also influence these pools. For phosphorus,

$$\frac{\partial[POP]}{\partial t} = -k_{pop}[POP] \tag{A.49}$$

$$\frac{\partial[DOP]}{\partial t} = -k_{dop}[DOP] \tag{A.50}$$

$$\frac{\partial[PO_4]}{\partial t} = k_{dop}[DOP] + k_{pop}[POP]. \tag{A.51}$$

For nitrogen,

$$\frac{\partial[PON]}{\partial t} = -k_{pon}[PON] \tag{A.52}$$

$$\frac{\partial[DON]}{\partial t} = -k_{don}[DON] \tag{A.53}$$

$$\frac{\partial[NH_4]}{\partial t} = k_{don}\,[DON] + k_{pon}\,[PON]. \tag{A.54}$$

And for silica and silicate,

$$\frac{\partial[PSi]}{\partial t} = -k_{psi}[PSi] \tag{A.55}$$

$$\frac{\partial\left[Si(OH)_4\right]}{\partial t} = k_{psi}[PSi]. \tag{A.56}$$

For nitrification, we define the light function,

$$\mathcal{I} = \begin{cases} 1-\frac{I_{PAR}}{I_0} & I_{PAR} \le I_0 \\ 0 & I_{PAR} > I_0 \end{cases} \tag{A.57}$$

which takes a value of 1 during darkness and 0 when PAR exceeds a critical value. Then

$$\frac{\partial[NH_4]}{\partial t} = -\mathcal{I}\,k_A[NH_4] \tag{A.58}$$

$$\frac{\partial[NO_2]}{\partial t} = \mathcal{I}\,(k_A[NH_4] - k_B[NO_2]) \tag{A.59}$$

$$\frac{\partial[NO_3]}{\partial t} = \mathcal{I}\,k_B[NO_2]). \tag{A.60}$$

Finally, sinking obeys the following relations:

$$\frac{\partial [P_i]}{\partial t} = -w_p \frac{\partial [P_i]}{\partial z} \quad \text{(A.61)}$$

$$\frac{\partial [POP]}{\partial t} = -w_{pom} \frac{\partial [POP]}{\partial z} \quad \text{(A.62)}$$

$$\frac{\partial [PON]}{\partial t} = -w_{pom} \frac{\partial [PON]}{\partial z} \quad \text{(A.63)}$$

$$\frac{\partial [PSi]}{\partial t} = -w_{pom} \frac{\partial [PSi]}{\partial z}. \quad \text{(A.64)}$$

Table A.1
Phytoplankton parameters for *Prochlorococcus*-like (PLP), small non-*Prochlorococcus*-like (SNP), large non-diatoms (LND), and diatom functional groups.

Parameter description	Symbol	Unit	PLP	SNP	LND	Diatom
Values governing randomized parameters						
Phosphate half saturation constant (min, max)	k_{PO4}	μM P	0.010, 0.015	0.015, 0.035	0.035, 0.055	0.035, 0.055
Nitrate half saturation constant (min, max)	k_{NO3}	μM N	0.16, 0.24	0.24, 0.56	0.56, 0.88	0.56, 0.88
Nitrite half saturation constant (min, max)	k_{NO2}	μM N	0.16, 0.24	0.24, 0.56	0.56, 0.88	0.56, 0.88
Ammonium half saturation constant (min, max)	k_{NH4}	μM N	0.08, 0.12	0.12, 0.28	0.28, 0.44	0.28, 0.44
Silicic acid half saturation constant	k_{Si}	μM Si	–	–	–	1
PAR half saturation (mean, standard deviation)	k_{par}	$(W m^{-2})^{-1}$	0.012, 0.02	0.012, 0.02	0.012, 0.006	0.012, 0.006
PAR inhibition (mean, standard deviation)	k_{inh}	$(W m^{-2})^{-1}$	0.006, 1e-4	0.006, 1e-4	0.001, 5e-5	0.001, 5e-5
Temperature optimum coefficient (min, max)	T_o	°C	5, 25	5, 25	5, 25	5, 25
Other fixed parameters						
Maximum growth rate	μ	d^{-1}	2.86	2.86	4.0	5.0
Temperature coefficient a	c_a	–	0.333	0.333	0.333	0.333
Temperature coefficient b	c_b	–	0.001	0.001	0.0003	0.0003
Temperature decay exponent	τ	–	4.000	4.000	4.000	4.000
Temperature decay scale	T_d	°C	5.62	5.62	7.60	7.60
Temperature normalization coefficient	T_n	–	0.300	0.300	0.300	0.300
Ammonium inhibition coefficient	σ_A	$(\mu M N)^{-1}$	4.6	4.6	4.6	4.6
Si:P elemental ratio	r_{SiP}	mol Si:mol P	–	–	–	16
N:P elemental ratio	r_{NP}	mol N:mol P	16	16	16	16
C:Chl	r_{CChl}	g C:g chl	300	300	100	50
Phytoplankton sinking rate	$w^{(P)}$	$m d^{-1}$	0.0	0.0	0.5	0.5
Phytplankton mortality rate	$m^{(P)}$	d^{-1}	0.1	0.1	0.1	0.1
Fraction of P mortality exported to particulates	$E^{(P)}$	–	0.2	0.2	0.5	0.5
Palatability by microzooplankton	$\pi^{(P)}$	–	1	1	0.4	0.28
Palatability by mesozooplankton	$\pi^{(P)}$	–	0.2	0.2	1	0.7
Grazing assimilation efficiency by microzoo	$\alpha^{(P)}$	–	0.500	0.500	0.200	0.200
Grazing assimilation efficiency by mesozoo	$\alpha^{(P)}$	–	0.700	0.700	0.500	0.500

Table A.2
Zooplankton parameters for microzooplankton and mesozooplankton.

Parameter description	Symbol	Unit	Microzoo	Mesozoo
Half saturation constant for grazing	k_g	μM P	0.04	0.07
Maximum grazing rate	G^{max}	d^{-1}	1.0	0.5
Grazing assimilation efficiency by mesozoo	$\alpha^{(Z)}$	–	0.3	–
Fraction of unassimilated prey exported to particulates	$E^{(G)}$	–	0.8	0.8
Zooplankton mortality	$m^{(Z)}$	d^{-1}	0.033	0.033
Fraction of Z mortality exported to particulates	$E^{(Z)}$	–	0.2	0.7

Table A.3
Other parameterizations: remineralization of dissolved and particulate organic matter, nitrification, and light attenuation.

Parameter description	Symbol	Unit	Value
DOP remineralization rate	k_{dop}	d^{-1}	0.020
DON remineralization rate	k_{don}	d^{-1}	0.020
POP remineralization rate	k_{pop}	d^{-1}	0.033
PON remineralization rate	k_{pon}	d^{-1}	0.033
PSi remineralization rate	k_{Psi}	d^{-1}	0.003
POM sinking rate	w_{pom}	$m d^{-1}$	10
Ammonium to nitrite oxidation rate	k_A	d^{-1}	0.1
Nitrite to nitrate oxidation rate	k_B	d^{-1}	0.033
Critical light level below which oxidation occurs	I_0	$W m^{-2}$	10
PAR attenuation coefficient	k_a	m^{-1}	0.04
PAR attenuation coefficent from phytoplankton	k_p	$(\mu M P m)^{-1}$	0.64

References

Anderson, G.C., 1969. Subsurface chlorophyll maximum in the northeast Pacific ocean. Limnol. Oceanogr. 14, 386–391.

Balech, E., 1960. The changes in the phytoplankton population off the California coast. The Changing Pacific Ocean in 1957 and 1958: Calif. Coop. Oceanic Fish. Invest. Rep., vol. 7, pp. 127–132.

Banas, N.S., Lessard, E.J., Kudela, R.M., MacCready, P., Peterson, T.D., Hickey, B.M., Frame, E., 2009. Planktonic growth and grazing in the Columbia River plume region: a biophysical model study. J. Geophys. Res. C 114.

Barber, R.T., Smith, R.L., 1981. Coastal Upwelling Ecosystems. Academic Press, p. 3168. Ch. 2.

Bolin, R.L., Abbott, D.P., 1963. Studies on the marine climate and phytoplankton of the central coastal area of California, 1954–1960. Calif. Coop. Oceanic Fish. Invest. Rep. 9, 23–45.

Brand, L.E., 1981. Genetic-variability in reproduction rates in marine-phytoplankton populations. Evolution 35 (6), 1117–1127.

Brand, L.E., Guillard, R.R.L., 1981. The effects of continuous light and light-intensity on the reproduction rates of 22 species of marine phytoplankton. J. Exp. Mar. Biol. Ecol. 50 (2–3), 119–132.

Broquet, G., Edwards, C.A., Moore, A.M., Powell, B.S., Veneziani, M., Doyle, J.D., 2009. Application of 4D-variational data assimilation to the California current system. Dyn. Atm. Oceans 48 (1–3), 69–92.

Bruland, K.W., Rue, E.L., Smith, G.J., 2001. Iron and macronutrients in California coastal upwelling regimes: implications for diatom blooms. Limnol. Oceanogr. 46 (7), 1661–1674.

Brush, M.J., Brawley, J.W., Nixon, S.W., Kremer, J.N., 2002. Modeling phytoplankton production: problems with the Eppley curve and an empirical alternative. Mar. Ecol. Prog. Ser. 238, 31–45.

Buck, K.R., Chavez, F.P., Campbell, L., 1996. Basin-wide distributions of living carbon components and the inverted trophic pyramid of the central gyre of the North Atlantic Ocean, summer 1993. Aquat. Microb. Ecol. 10 (3), 283–298.

Campbell, L., Nolla, H.A., Vaulot, D., 1994. The importance of *Prochlorococcus* to community structure in the central North Pacific. Limnol. Oceanogr. 39, 954–961.

Chai, F., Dugdale, R.C., Peng, T.H., Wilkerson, F.P., Barber, R.T., 2002. One-dimensional ecosystem model of the equatorial Pacific upwelling system. Part I: model development and silicon and nitrogen cycle. Deep-Sea Res. II 49 (13–14), 2713–2745.

Chan, A.T., 1978. Comparative physiological study of marine diatoms and dinoflagellates in relation to irradiance and cell-size. I. Growth under continuous light. J. Phycol. 14 (4), 396–402.

Chan, A.T., 1980. Comparative physiological study of marine diatoms and dinoflagellates in relation to irradiance and cell-size. 2. Relationship between photosynthesis, growth, and carbon-chlorophyll a-ratio. J. Phycol. 16 (3), 428–432.

Chang, J., Shiah, F.K., Gong, G.C., Chiang, K.P., 2003. Cross-shelf variation in carbon-to-chlorophyll a ratios in the East China Sea, summer 1998. Deep-Sea Res. II 50 (6–7), 1237–1247.

Chavez, F.P., Buck, K.R., Service, S.K., Newton, J., Barber, R.T., 1996. Phytoplankton variability in the central and eastern tropical Pacific. Deep-Sea Res. II 43 (4–6), 835–870.

Chavez, F.P., Pennington, J.T., Castro, C.G., Ryan, J.P., Michisaki, R.P., Schlining, B., Walz, P., Buck, K.R., McFadyen, A., Collins, C.A., 2002. Biological and chemical consequences of the 1997–1998 El Niño in central California waters. Prog. Oceanogr. 54 (1–4), 205–232.

Checkley Jr., D.M., Barth, J.A., 2009. Patterns and processes in the California Current System. Prog. Oceanogr.

Collier, J.L., Palenik, B., 2003. Phycoerythrin-containing picoplankton in the Southern California Bight. Deep-Sea Res. II 50, 2405–2422.

Conway, H.L., 1977. Interactions of inorganic nitrogen in uptake and assimilation by marine-phytoplankton. Mar. Biol. 39 (3), 221–232.

Cowles, T.J., Olson, R.J., Chisholm, S.W., 1988. Food selection by copepods: discrimination on the basis of food quality. Mar. Biol. 100 (1), 41–49.

Cullen, J.J., Eppley, R.W., 1981. Chlorophyll maximum layers of the Southern California Bight and possible mechanisms of their formation and maintenance. Oceanol. Acta 4, 23–32.

Cullen, J.J., Reid, F.M.H., Stewart, E., 1982. Phytoplankton in the surface and chlorophyll maximum off southern California in August, 1978. J. Plankton Res. 4, 665–693.

Dugdale, R.C., Goering, J.J., 1967. Uptake of new and regenerated forms of nitrogen in primary productivity. Limnol. Oceanogr. 12, 196–206.

Edwards, C.A., Batchelder, H.P., Powell, T.M., 2000a. Modeling microzooplankton and macrozooplankton dynamics within a coastal upwelling system. J. Plankton Res. 22, 1619–1648.

Edwards, C.A., Powell, T.A., Batchelder, H.P., 2000b. The stability of an NPZ model subject to realistic levels of vertical mixing. J. Mar. Res. 58 (1), 37–60.

Eppley, R.W., 1972. Temperature and phytoplankton growth in the sea. Fish Bull. 70 (4), 1063–1085.

Eppley, R.W., Coatsworth, J.L., Solorzano, L., 1969. Studies of nitrate reductase in marine phytoplankton. Limnol. Oceanogr. 14, 194–205.

Fennel, K., Boss, E., 2003. Subsurface maxima of phytoplankton and chlorophyll: steady-state solutions from a simple model. Limnol. Oceanogr. 48, 1521–1534.

Finkel, Z.V., 2001. Light absorption and size scaling of light-limited metabolism in marine diatoms. Limnol. Oceanogr. 46 (1), 86–94.

Flynn, K.J., Davidson, K., Cunningham, A., 1996. Prey selection and rejection by a microflagellate; implications for the study and operation of microbial food webs. J. Exp. Mar. Biol. Ecol. 196 (1–2), 357–372.

Follows, M.J., Dutkiewicz, S., Grant, S., Chisholm, S.W., 2007. Emergent biogeography of microbial communities in a model ocean. Science 315 (5820), 1843–1846.

Franks, P.J.S., Wroblewski, J.S., Flierl, G.R., 1986. Behavior of a simple plankton mod with food-level acclimation by herbivores. Mar. Biol. 91, 121–129.

Furnas, M.J., 1990. In situ growth-rates of marine-phytoplankton — approaches measurement, community and species growth-rates. J. Plankton Res. 12 (6 1117–1151.

Furnas, M.J., 1991. Net in situ growth rates of phytoplankton in an oligotrophic, tropic shelf ecosystem. Limnol. Oceanogr. 36 (1), 13–29.

Gallegos, C.L., Vant, W.N., 1996. An incubation procedure for estimating carbon-t chlorophyll ratios and growth-irradiance relationships of estuarine phytoplankto Mar. Ecol. Prog. Ser. 138 (1–3), 275–291.

Garrison, D.L., 1979. Monterey Bay phytoplankton I. Seasonal cycles of phytoplankt assemblages. J. Plankton Res. 1 (3), 241–266.

Geider, R.J., 1987. Light and temperature-dependence of the carbon to chlorophyll ratio in microalgae and cyanobacteria — implications for physiology and growth phytoplankton. New Phytol. 106 (1), 1–34.

Geider, R.J., La Roche, J., 2002. Redfield revisited: variability of C:N:P in mari microalgae and its biochemical basis. Eur. J. Phycol. 37 (1), 1–17.

Geider, R.J., McIntyre, H.L., Kana, T.M., 1996. A dynamic model of photoadaptation phytoplankton. Limnol. Oceanogr. 41, 1–15.

Gentleman, W., Leising, A., Frost, B., Strom, S., Murray, J., 2003. Functional responses zooplankton feeding on multiple resources: a review of assumptions and biologic dynamics. Deep-Sea Res. II 50, 2847–2875.

Gruber, N., Frenzel, H., Doney, S.C., Marchesiello, P., McWilliams, J.C., Moisan, J.R., Ora J.J., Plattner, G.K., Stolzenbach, K.D., 2006. Eddy-resolving simulation of plankt ecosystem dynamics in the California Current System. Deep-Sea Res. I 1483–1516.

Haidvogel, D.B., Beckman, A., 1999. Numerical Ocean Circulation Modeling. Imper Coll. Press, River Edge, N.J.

Harrison, W.G., 1976. Nitrate metabolism of red tide dinoflagellate Gonyaulax–Polyed Stein. J. Exp. Mar. Biol. Ecol. 21 (3), 199–209.

Hickey, B.M., Banas, N.S., 2008. Why is the northern end of the California Curr System so productive? Oceanography 21 (4), 90–107.

Hood, R.R., Abbott, M.R., Huyer, A., 1991. Phytoplankton and photosynthetic lig response in the Coastal Transition Zone off Northern California in June 1987 Geophys. Res. 96, 14769–14780.

Hutchins, D.A., Bruland, K.W., 1998. Iron-limited diatom growth and Si:N uptake rat in a coastal upwelling regime. Nature 393 (6685), 561–564.

Hutchinson, G.E., 1961. The paradox of the plankton. Am. Nat. 95 (882), 137–145.

Johnson, Z.I., Zinser, E.R., Coe, A., McNulty, N.P., Woodward, E.M.S., Chisholm, S. 2006. Niche partitioning among *Prochlorococcus* ecotypes along ocean-sc environmental gradients. Science 311 (5768), 1737–1740.

Leising, A.W., Pierson, J.J., Halsband-Lenk, C., Horner, R., Postel, J., 2005a. Copep grazing during spring blooms: can *Pseudocalanus newmani* induce trop cascades? Prog. Oceanogr. 67 (3–4), 406–421.

Leising, A.W., Pierson, J.J., Halsband-Lenk, C., Horner, R., Postel, J., 2005b. Copep grazing during spring blooms: does *Calanus pacificus* avoid harmful diatoms? Pr Oceanogr. 67 (3–4), 384–405.

L'Helguen, S., Maguer, J.-F., Caradec, J., 2008. Inhibition kinetics of nitrate uptake ammonium in size-fractionated oceanic phytoplankton communities: implicati for new production and *f*-ratio estimates. J. Plankton Res. 30 (10), 1179–1188.

Litchman, E., Klausmeier, C.A., Miller, J.R., Schofield, O.M., Falkowski, P.G., 2006. Mu nutrient, multi-group model of present and future oceanic phytoplank communities. Biogeosciences 3 (4), 585–606.

Litchman, E., Klausmeier, C.A., Schofield, O.M., Falkowski, P.G., 2007. The role functional traits and trade-offs in structuring phytoplankton communities: scal from cellular to ecosystem level. Ecol. Lett. 10, 1170–1181.

Marra, J., Barber, R.T., 2004. Phytoplankton and heterotrophic respiration in the surf layer of the ocean. Geophys. Res. Lett. 31 (9).

Moisan, J.R., Moisan, T.A., Abbott, M.R., 2002. Modelling the effect of temperature on maximum growth rates of phytoplankton populations. Ecol. Model. 153, 197–2

Moore, J.K., Doney, S.C., Kleypas, J.A., Glover, D.M., Fung, I.Y., 2002a. An intermed complexity marine ecosystem model for the global domain. Deep-Sea Res. II 49 (1 403–462.

Moore, L.R., Post, A.F., Rocap, G., Chisholm, S.W., 2002b. Utilization of different nitro sources by the marine cyanobacteria *Prochlorococcus* and *Synechococcus*. Lim Oceanogr. 47 (4), 989–996.

Nianzhi, J., 1993. Interactions between ammonium uptake and nitrate uptake natural phytoplankton assemblages. Chin. J. Oceanol. Limnol. 11 (2), 97–107.

O'Reilly, J.E., Maritorena, S., Mitchell, B.G., Siegel, D.A., Carder, K.L., Garver, S.A., Ka M., McClain, C., 1998. Ocean color chlorophyll algorithms for SeaWiFS. J. Geop Res. 103 (C11), 24937–24953.

Plattner, G.K., Gruber, N., Frenzel, H., McWilliams, J.C., 2005. Decoupling marine ex production from new production. Geophys. Res. Lett. 32 (11).

Powell, T.M., Lewis, C.V.W., Curchitser, E.N., Haidvogel, D.B., Hermann, A.J., Dobbins, 2006. Ecosystem response to upwelling off the Oregon Coast: behavior of t nitrogen-based models. J. Geophys. Res. C 111.

Putland, J.N., Iverson, R.L., 2007. Phytoplankton biomass in a subtropical estu distribution, size composition, and carbon:chlorophyll ratios. Estuar. Coasts 30 878–885.

Rabouille, S., Edwards, C.A., Zehr, J.P., 2007. Modelling the vertical distributio *Prochlorococcus* and *Synechococcus* in the North Pacic Subtropical Ocean. Envi Microbiol. 9, 2588–2602.

Riemann, B., Simonsen, P., Stensgaard, L., 1989. The carbon and chlorophyll conte phytoplankton from various nutrient regimes. J. Plankton Res. 11 (5), 1037–1

Roy, S., Chattopadhyay, J., 2007. Enrichment and ecosystem stability: effect of food. Biosystems 90 (1), 151–160.

Sathyendranath, S., Stuart, V., Nair, A., Oka, K., Nakane, T., Bouman, H., Forget, M.-H., Maass, H., Platt, T., 2009. Carbon-to-chlorophyll ratio and growth rate of phytoplankton in the sea. Mar. Ecol. Prog. Ser. 383, 73–84.
Shen, E.B., Sherr, B.F., Wheeler, P.A., 2005. Distribution of coccoid cyanobacteria and small eukaryotic phytoplankton in the upwelling ecosystem off the Oregon coast during 2001 and 2002. Deep-Sea Res. II 52 (1–2), 317–330.
Smolarkiewicz, P.K., Margolin, L.G., 1998. MPDATA: a finite-difference solver for geophysical flows. J. Comput. Phys. 140 (2), 459–480.
Spitz, Y.H., Newberger, P.A., Allen, J.S., 2003. Ecosystem response to upwelling off the Oregon coast: behavior of three nitrogen-based models. J. Geophys. Res. C 108.
Strub, P.T., Allen, J.S., Huyer, A., Smith, R.L., 1987. Large-scale structure of the spring transition in the coastal ocean off western North America. J. Geophys. Res. 92, 1527–1544.
Taylor, K.E., 2001. Summarizing multiple aspects of model performance in a single diagram. J. Geophys. Res. D 106 (D7), 7183–7192.
Veldhuis, M.J.W., Kraay, G.W., 2004. Phytoplankton in the subtropical Atlantic ocean: towards a better assessment of biomass and composition. Deep-Sea Res. I 51 (4), 507–530.
Veldhuis, M.J.W., Timmermans, K.R., Croot, P., van der Wagt, B., 2005. Picophytoplankton; a comparative study of their biochemical composition and photosynthetic properties. J. Sea Res. 53 (1–2), 7–24.
Veneziani, M., Edwards, C.A., Doyle, J.D., Foley, D., 2009a. A central California coastal ocean modeling study: 1. Forward model and the influence of realistic versus climatological forcing. J. Geophys. Res. C 114.
Veneziani, M., Edwards, C.A., Moore, A.M., 2009b. A central California coastal ocean modeling study: 2. Adjoint sensitivities to local and remote forcing mechanisms. J. Geophys. Res. C 114.
Venrick, E.L., 2009. Floral patterns in the California Current: the coastal-offshore boundary zone. J. Mar. Res. 67 (1), 89–111.
Venrick, E.L., McGowan, J.A., Mantyla, A.W., 1973. Deep maxima of photosynthetic chlorophyll in the Pacific Ocean. Fish Bull. 71, 41–52.
Verity, P.G., Smetacek, V., 1996. Organism life cycles, predation, and the structure of marine pelagic ecosystems. Mar. Ecol. Prog. Ser. 130 (1–3), 277–293.
Weiler, C.S., Eppley, R.W., 1979. Temporal pattern of division in the dinoflagellate genus *Ceratium* and its application to the determination of growth rate. J. Exp. Mar. Biol. Ecol. 39 (1), 1–24.
Worden, A.Z., Nolan, J.K., Palenik, B., 2004. Assessing the dynamics and ecology of marine picophytoplankton: the importance of the eukaryotic component. Limnol. Oceanogr. 49 (1), 168–179.